UNIVERSITÀ DEGLI STUDI DI PADOVA

Dipartimento di Fisica e Astronomia "Galileo Galilei"

Master Degree in Astrophysics and Cosmology

Final Dissertation

Spectral analysis of the multiple populations in Omega Centauri with MUSE

Thesis supervisor
Prof. Antonino P. Milone
Thesis co-supervisor
Dr. Nadine Neumayer

Candidate
Simona Di Stefano

Academic Year 2022/23

Abstract

Globular clusters are spherical stellar clusters, containing up to millions of old stars which are typically metal-poor. They are so old that they are even used to give estimates of the age of the Universe itself and, for a long time, they were considered as the best example of simple stellar populations. However, since the presence of multiple stellar populations was confirmed in both the Galactic and extra-galactic environment, globular clusters now represent a main challenge: characterizing the formation and the evolution of their populations is still an open issue in the astrophysical research. The most extreme and massive case in our Galaxy is represented by ω Centauri: the disentanglement of its huge number of stellar populations and the determination of their ages and chemistry have proven to be particularly challenging for decades. Given this complexity, ω Centauri is believed to be the nuclear star cluster of an accreted dwarf satellite of the Milky Way.

The aim of this thesis is to analyze the spectra of the most massive Galactic globular cluster, with a particular focus on 5278 red giant branch (RGB) stars within its core radius, in order to qualitatively compare the chemical features of ω Centauri's nine populations. The spectra are taken with the *Multi Unit Spectroscopic Explorer* (MUSE) at the Very Large Telescope (VLT), whereas the populations have been previously identified by taking advantage of the *Hubble Space Telescope* (HST) photometry. To do this analysis, the technique of spectral stacking is applied: hundreds of individual spectra are combined into a single S/N-averaged "stacked" spectrum, which is representative of each population. The stacking is performed not only per population, but also per magnitude bin, so as to combine stars with more homogeneous atmospheric parameters and to confirm that the chemical properties of a specific population do not depend on stellar magnitude.

After normalizing the stacked spectra to the continuum, a closer look at the most prominent absorption lines reveals that the populations have different line depths of many metals, such as Mg, Ca, Ba, Al and Na. Consequently, the spectral stacking proves to be an effective technique that makes abundance measurements accessible, in spite of the low S/N of the individual low resolution MUSE spectra.

After developing this thesis, an accurate quantitative determination of the elemental abundances, by means of spectral synthesis, is forthcoming.

Contents

Introduction

1.1 Multiple populations in Globular Clusters

Globular clusters (GCs) are among the oldest and most metal poor objects that can be found in a galaxy. They can be considered as fossils in galactic archaeology of the Local Universe and used to shed light on the Primordial Universe (e.g. Frebel & Norris 2015). Moreover, they are thought to play a key role in the assembly of the Galactic halo. For a long time, astronomers considered the GCs as the best example of simple stellar populations (SSPs), where all the stars are characterized by the same metallicity, age and initial mass function (IMF), and formed in a single star formation burst (e.g. Renzini & Buzzoni 1986). Nonetheless, the discoveries of the past few decades have shown that multiple stellar populations (MPs) are commonly found in both Galactic and extragalactic GCs (see Bastian & Lardo 2018, Gratton et al. 2012, Gratton et al. 2019, Milone & Marino 2022 for recent reviews).

However, understanding the formation and evolution of these populations is still very puzzling and represents an open issue in the fields of stellar evolution and stellar nucleosynthesis (Milone & Marino, 2022). What is evident since the late 1990s is that photometry is an efficient tool to identify MPs among stars at different evolutionary phases: split or broad main sequences (MSs, see Fig. 1.1, *right*), red giant branches (RGBs, see Fig. 1.1, *left*) and sub-giant branches (SGBs) started to seem all quite common features in color magnitude diagrams (CMDs) of GCs (e.g. Milone et al. 2008), and soon it became evident that the multiple sequences can be followed continuously in all evolutionary stages (Milone & Marino, 2022).

In particular, the splitting of the sequences in the CMDs is possibly caused by a difference in helium and light element abundances and, in the most extreme cases, heavy element content as well. According to various scenarios on GCs formation, multiple stellar populations could correspond to different stellar generations, with multiple star formation
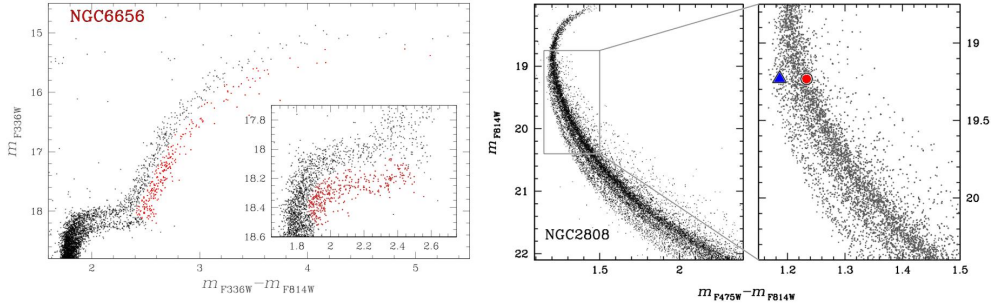
Figure 1.1: *Left*: the split RGB and SGB in NGC 6656, with the red dots indicating the redder component (Milone et al., 2017). *Right*: the triple MS in NGC 2808, where the blue triangle and the red circle are used to distinguish the bluer and the redder sequence respectively (Bragaglia et al., 2010).

events taking place: while the first burst would form stars out of pristine material, the following one (or more) would form stars out of the polluted ashes that come from these more massive first-populations stars, which evolve faster (Cottrell & Da Costa, 1981; Dantona et al., 1983). The result is that a first generation of stars (hereafter 1P) and one or more second stellar generations (2P) can be distinguished: while the first resemble field stars with similar metallicities, the second shows a signature of high-temperature hydrogen burning, resulting in the enhancement in elements such as He, N, Na and Al and the depletion in C and O (Milone & Marino, 2022); this enrichment typically sets precise light element abundance patterns, such as the Na-O and C-N anticorrelations (Fig. 1.3) and the observed star-to-star variations in some light elements suggest a certain degree of self-enrichment within the globular clusters' environment (Carretta et al., 2009).

In order to disentangle the populations according to their light element abundances, Milone et al. (2015) introduced a pseudo two-color diagram - the Chromosome Map (ChM) - that can be effectively built for stars in the MS, RGB or AGB. This diagram maximizes the separation among the discrete populations by using a combination of filters that are sensitive to the variations in some specific elements, such as He and N, so that, with respect to a simple two-color diagram, the stars are verticalized in both dimensions, concentrating the single population to which they belong in a small area of the ChM. Hence, two types of GCs have been identified in the literature (e.g. Marino et al. 2009):

- **Type I GCs**, that is, the majority of Galactic GCs. They host 1P and 2P stars which differ for light element abundances. An example of ChM for a Type I GC is reported in Fig. 1.2.

- **Type II GCs**. They represent around 15%-20% of the Galactic GCs, and share the
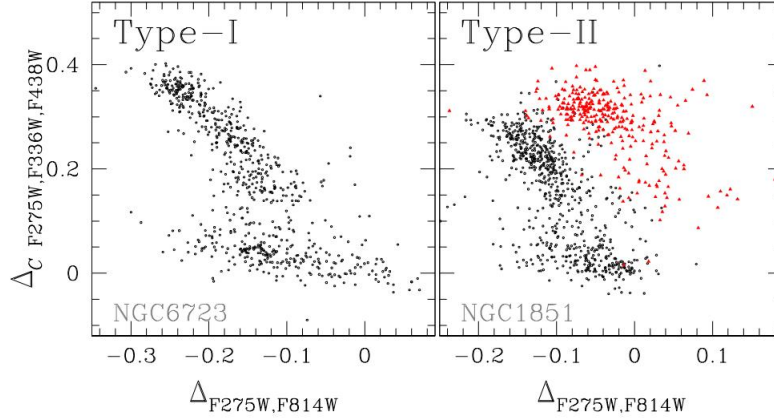
8

Figure 1.2: Chromosome maps of NGC 6723 and NGC 1851, which are two prototypes of Type I and Type II GCs respectively (Milone et al., 2017; Milone & Marino, 2022). Red symbols mark the red RGB stars of NGC 1851.
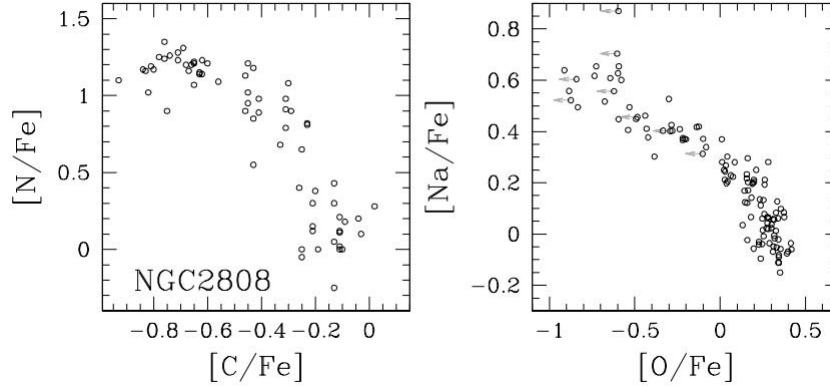

Figure 1.3: C-N and Na-O anticorrelations found in NGC 2808 (Milone & Marino, 2022).

following properties (possibly physically related to each other):

1. They show at least an additional sequence on the red side of the ChM (see Fig. 1.2);

2. they have a split or broad subgiant branch (SGB) in both UV and optical CMDs;

3. they exhibit significant variation in metallicity, due to iron content variation or overall C+N+O variation, or both.
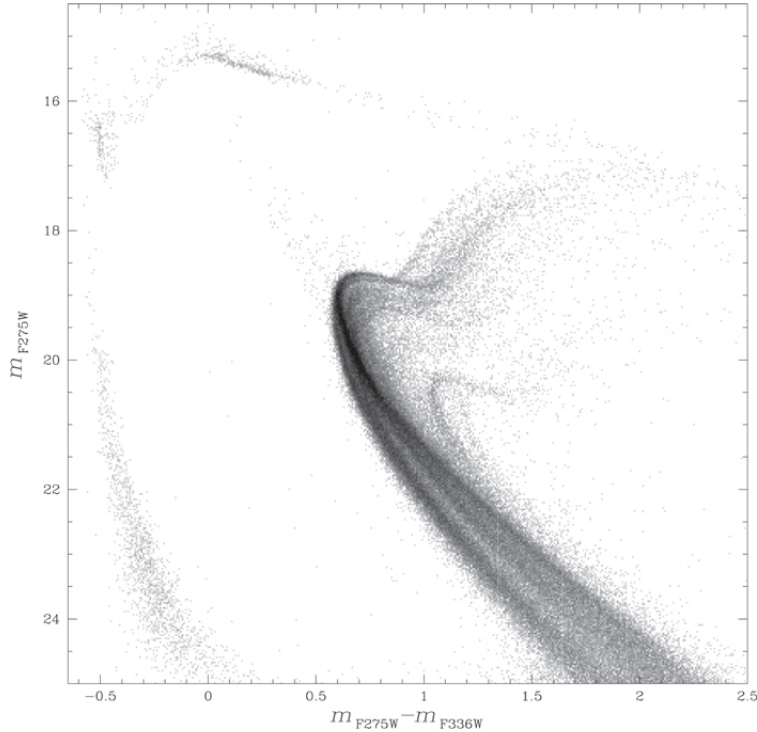
Figure 1.4: The CMD of ω Cen from Bellini et al. (2017a), in the F275W versus F275W $-$ F336W filters. The multiple streams are clearly visible at different evolutionary stages.

1.2 Omega Centauri as a type II Globular Cluster

Omega Centauri (ω Cen) is certainly the most extreme, enigmatic and massive Galactic GC: with its mass estimated as $\sim 3.5 \cdot 10^6 M_\odot$ (Baumgardt & Hilker, 2018), this cluster is well known to host a high number of multiple stellar populations - at least 16, as found by Marino et al. 2019 - which are characterized by a significant spread in metallicity ($-2.2 \leq$ [Fe/H] ≤ -0.6, e.g. Johnson & Pilachowski 2010) and light element abundances. The age distribution of the stellar populations in ω Cen is controversial. Some authors suggest a wide age spread that ranges from less than 2 Gyr (Joo & Lee, 2013) to more than 4 Gyr (Hilker et al., 2004). However, recent work, that account for the observed C+N+O variations favour a smaller age spread, with the most metal-rich stellar populations being slightly younger than the metal-poor ones (e.g. Marino et al. 2012, Tailo et al. 2015). A decade ago, ω Cen was believed to be the only case of globular cluster hosting multiple populations in the CMD (Anderson, 1997) and was thus initially addressed as a transition object between clusters and galaxies or even suspected to be the merger of two clusters. Then, as the photometric studies became more and more precise (e.g. thanks to the advent of *Hubble Space Telescope*, HST), it became clear that the phenomenon of MPs was not a

peculiarity of this object, but an example of self-enrichment by which most of GCs are affected, and of which this target is just the most extreme representative case (Bellini et al., 2017a).

However, due to the complexity of its MPs, the star formation history of ω Cen is currently poorly understood. For this reason, some theories support the scenario of it being the stripped nuclear star cluster of an accreted dwarf satellite of our Galaxy.

1.2.1 The stripped nucleus scenario

It is currently reported by many authors that what we consider massive Galactic globular clusters could actually be dwarf galaxies in disguise or, better, the nuclear star clusters (NSCs) that are found in their centers (Norris & Da Costa, 1995; Da Costa & Marino, 2011; Pfeffer et al., 2021). When a merger event happens, these structures survive and keep on living in the galactic halo of the larger galaxy. Moreover, NSCs may share some properties with GCs (Neumayer et al., 2020), as the range of masses (from $10^6 M_\odot$ to $10^8 M_\odot$) and half light radii (from 1 pc to 10 pc), which is in agreement with the fact that they could actually look like massive GCs. Most importantly, they are known to show clear evidence for multiple generations of star formation and/or extended star formation histories, which can be due to an extended *in situ* star formation (Seth et al., 2006) or even to the merging of multiple GCs (Capuzzo-Dolcetta, 1993). These traits are consequently visible in the CMDs and spectroscopic observations of the NSCs, both as spread in heavy elements and as prolonged star formation histories.
With such a large assortment of MPs and their spread in [Fe/H], ω Cen is thought to actually be the nuclear star cluster of an old dwarf satellite that was orbiting the Milky Way and was then tidally disrupted, i.e. the remnant of a large building block of the Galaxy (Massari et al., 2019; Pfeffer et al., 2021). Therefore, this target is the ideal case to shed light on the connection between GCs and dwarf galaxies for the following reasons:

- it's very close to us ($\sim$ 5 kpc). If it was a NSC, it could be the perfect case study concerning these objects;

- the masses and star formation histories of NSCs are related to the ones of the galaxy they live in, therefore from stripped nuclei we can infer the mass of the original host and the time of merging (Neumayer et al., 2020). This means that ω Cen would allow to shed light on the assembly history of the Milky Way itself.

Recently, the advent of the *Gaia* mission (Gaia Collaboration et al., 2016) allowed to dynamically trace the origin of the majority of Galactic GCs, revealing numerous streams and debris that help to reconstruct the Milky Way's accretion history. In particular, ω Cen is generally associated to the old center of the Gaia-Enceladus dwarf galaxy, due to the

kinematics and age-metallicity relations that have been found (Pfeffer et al., 2021). The cluster's retrograde motion is a strong evidence of this capture theory, implying that the object was more massive in the past (Dinescu et al., 1999). Furthermore, recent studies by Ibata et al. (2019) associate it to the "Fimbulthul" stellar stream, as a trace of its tidal debris spread along the orbit.

1.2.2 Omega Centauri in the recent literature

Finding the number and the mean metallicity of the subpopulations in ω Cen has been a main challenge for decades. One of the initial discoveries was a bimodal distribution of [Ca/H] in the RGB, based on low-resolution spectra, being in particular the first peak at [Ca/H] ~ -1.4 and the second at [Ca/H] ~ -1.0 (Norris et al., 1996). Soon, Bedin et al. (2004) confirmed the existence of a double MS branch as well, in which later studies found the bluer branch to be more metal-rich than the red one. This behaviour, that was against any expectation from canonical stellar models, was explained with a high He content in the bluer sequence (Piotto et al., 2005).
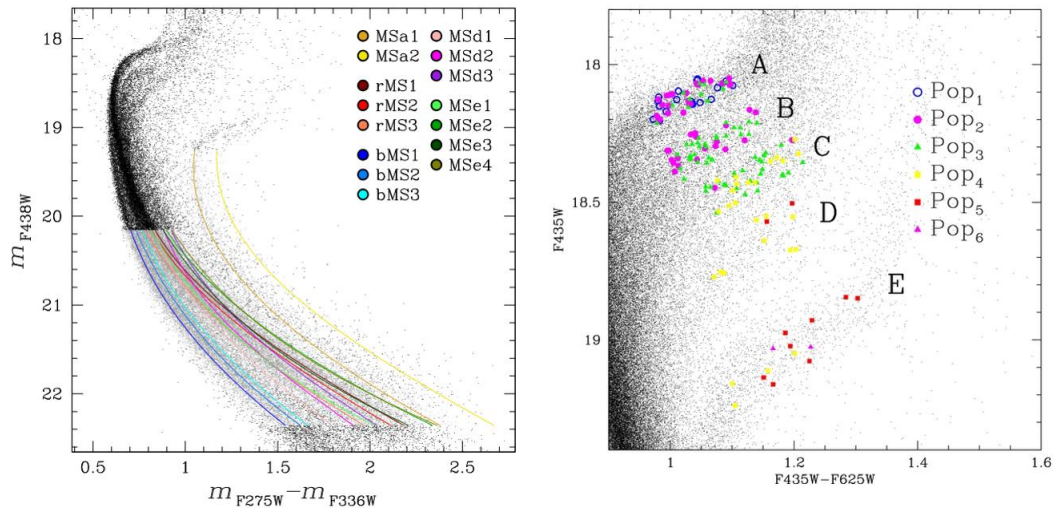

Figure 1.5: *Left*: the 15 MS subpopulations identified by Bellini et al. (2017b). *Right*: the 6 SGB subpopulations identified by Villanova et al. (2014).

In time, the number of stellar populations in ω Cen increased more and more, as the blue and red MS branches were both found to hide further stellar subpopulations. Yet, the most recent observational studies focus just on specific sections of the CMD, such as the MS (e.g. Bellini et al. 2017b and their catalog Bellini et al. 2017a), the SGB (Villanova et al., 2014) and the RGB (as in Milone et al. 2017 and Marino et al. 2019), so that, overall, ω Cen is known to exhibit star-to-star variations in several light elements, such as

C, N, O, Na, Mg, Al and Si, and even in s-process elements (e.g. Johnson & Pilachowski 2010); moreover, it shows the typical light element abundance patterns that are commonly found in Galactic GCs, as the Na-O and C-N anticorrelations, according to the chemical enrichment process expected in the 2P with respect to the 1P stars. These anticorrelations are present within stellar populations with different metallicity (Johnson & Pilachowski, 2010).

On one hand, Villanova et al. (2014) went deeper into the investigation of the age-metallicity relation by analyzing the spectra of 172 stars in the SGB of the cluster. They identified six subpopulations with different [Fe/H] (Fig. 1.5 *right*), being the value of the most metal-poor [Fe/H] ~ -2.0 and the one of the most metal-rich [Fe/H] ~ -1.2. However, since the oldest stars in the metal-rich regime seemed to be several Gyrs older than their oldest metal-poor counterparts, the authors excluded any kind of chemical evolution between the two, hypothesizing the scenario of merging between two independent primordial populations.

On the other hand, Bellini et al. (2017b) built a comprehensive catalog of photometry and proper motions for the target's core ($\sim 2'.37$), including more than 470,000 stars and collecting more than 650 multi-epoch exposures. The images were taken with WFC3/UVIS and WFC3/IR on board HST, for a total of 26 distinct filters, such as F275W, F336W, F438W, F606W and F814W. By analyzing the CMDs and the Chromosome Maps of the MS, taking advantage of the combinations of different filters, up to 15 subpopulations were identified (Fig. 1.4 and Fig. 1.5 *left*).
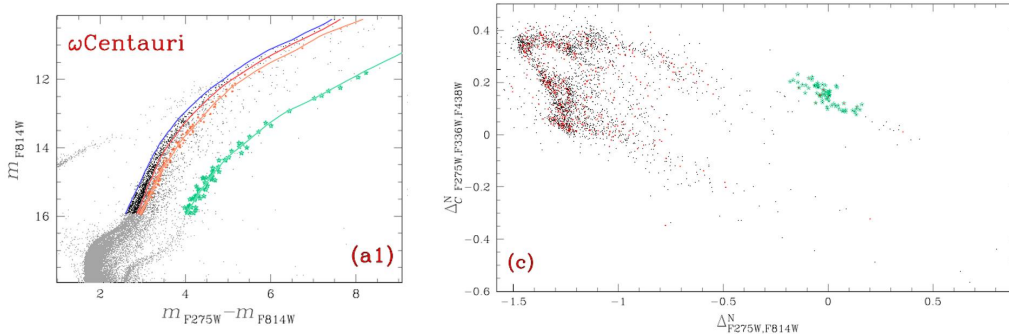

Figure 1.6: The RGB subpopulations identified by Milone et al. (2017) (*left*) and the corresponding ChM (*right*).

Eventually, results by Milone et al. (2017) showed how complex the ChM of the RGB can be. With a suitable combination of colors and pseudo-colors, they distinguished three main groups of stars, and each of these is related to multiple - and difficult to disentangle - additional bumps of stars (see Fig. 1.6, *right*). In particular, the third, reddest group of stars (marked with aqua-starred symbols in Fig. 1.6) represents the most metal-rich stellar

stream in the RGB of the cluster. In Marino et al. (2019), the number of subpopulations in the RGB is estimated as 16, with the most metal-rich stars generally found to be enhanced in Na, Al and depleted in Li: among them, those that belong to the blue RGB (likely corresponding to 2P) show less extreme abundances in these elements, while the metal-rich, red RGB have the most extreme enrichment in Na, Al and depletion in Li and are likely to be the most enhanced in He as well.

1.3 Thesis layout

The aim of the thesis is to compare the average chemical properties of the MPs in ω Cen, by comparing their stacked spectra. Spectral stacking is a technique applied in Latour et al. (2019) with the purpose of increasing the signal-to-noise ratio (S/N) of individual spectra by combining thousands of them in a single one, which is representative of the single population. In this way, it is possible to draw qualitative conclusions on the chemical enrichment history of the object, and potentially to shed light on its possible connection with a dwarf galaxy.

After describing the phenomenon of MPs in GCs, with a particular focus on ω Cen and the corresponding observational findings and challenges, the thesis is structured as follows:

- ↪ **Data reduction**: here is an explanation of the MUSE dataset used for the spectral analysis of the MPs in ω Cen and of the previous work done to identify the populations starting from archival HST photometry. All the corrections applied to the individual spectra are explained, up to the creation of the stacked spectra, that are analyzed in the next section.

- ↪ **Data analysis**: the spectra of each subpopulation are stacked per magnitude bin, normalized and shown in panels. An estimate for the mean metallicity of each populations is provided as well.

- ↪ **Discussion and conclusions**: here the most prominent lines in the stacked spectra are zoomed in. These lines, such as Mg and Ca triplets, are crucial to understand, at least qualitatively, how the chemical enrichment process is developed among the different subpopulations. The results of the thesis are then summarized and some qualitative conclusions are drawn.

Data reduction

2.1 Dataset

The dataset analyzed in the thesis consists of 5278 stars that populate the central region of ω Cen (Fig. 2.1), covering out to the core radius of the cluster ($r_{\rm c} \simeq 2'.37$, red circle in Fig. 2.1). This dataset comes from the combination of two catalogs: the MUSE spectral catalog by M. S. Nitschai (Nitschai et al., 2023), that couples the spectra with the HST photometry by Anderson & van der Marel (2010), and the clustering catalog by C. Clontz (Clontz et al., in prep.), which uses the archival HST photometric catalog by Bellini et al. (2017a) to assign stars to their respective stellar population. While the MUSE spectral catalog covers out to the half-light radius of ω Cen ($r_{\rm hl} \simeq 4'.65$, green circle in Fig. 2.1), the clustering catalog limits the thesis sample to the core radius of the target, being limited to Bellini et al. (2017a) photometry.

In the following, the methods of data analysis and data reduction are described. Specifically, Sect. 2.1.1 is focused on the spectroscopic dataset and the methods to reduce MUSE spectra, whereas Sect. 2.1.2 describes the methods used to disentangle the main stellar populations of ω Cen. The analysis of the individual MUSE spectra is provided in Sect. 2.2, while Sect. 2.3 is dedicated to the determination of the stacked spectra for stars in each stellar population.

2.1.1 MUSE dataset and spectroscopic data reduction

The spectra analyzed in this thesis are taken with the *Multi Unit Spectroscopic Explorer* MUSE (Bacon et al. 2010, Bacon et al. 2014), namely the integral-field unit spectrograph at the Very Large Telescope (VLT) in Chile (Paranal Observatory), and are part of a much larger spectroscopic dataset (Nitschai et al., 2023) which, in turn, comes from the combination of:

- "GTO data": a set of existing data, taken from part of the MUSE Guaranteed Time
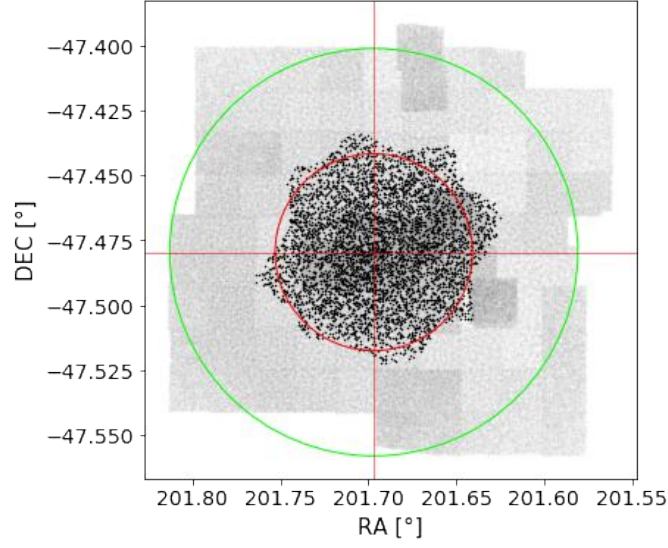
Figure 2.1: Right ascension (RA) and declination (DEC) of the sample of stars analyzed in this thesis (*black*). Grey regions indicate all the field of view covered by MUSE pointings within the overall GTO and GO datasets. The red circle marks the core radius of the target ($r_c \simeq 2'.37$), whereas the green one marks its half-light radius ($r_{hl} \simeq 4'.65$).
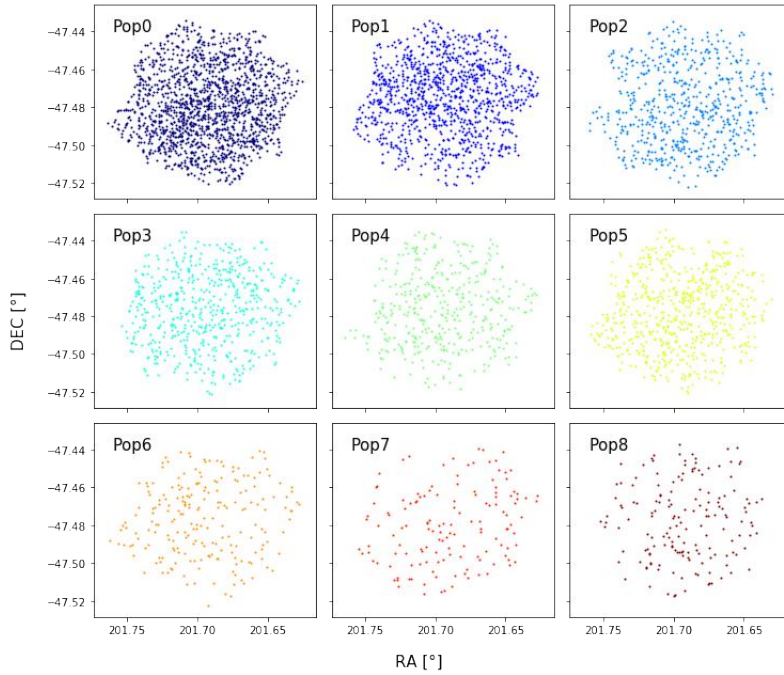

Figure 2.2: RA and DEC of the nine populations.

Observation, consisting of 10 pointings with multi-epoch data in the wide field mode (WFM) - already analyzed in the literature, e.g. Kamann et al. (2018), Latour et al. (2021) - plus 6 central pointings adopting the narrow field adaptive optics mode (NFM) - presented in Pechetti et al. (2023). In particular, the IDs of the first 10 pointings are: 094.D-155 0142, 095.D-0629, 096.D-0175, 097.D-0295, 098.D-0148, 156 099.D-0019, 0100.D-0161, 0101.D-0268, 0102.D-0270, 157 0103.D-0204, 0104.D-0257, 105.20CR, and 109.23DV.

- "GO data": a set of data from the Guest Observers program 105.CG.001 (PI: N. Neumayer), made of 87 new pointings in total taken from February 2021 to September 2022. GO data use the wide field mode (WFM) of the instrument.

The total number of stars in the extended catalog is about ∼300,000, covering out to the half-light radius of the target (Fig. 2.1).
The MUSE spectrograph observes in the optical window, from 4800 Å to 9300 Å, and with a spectral sampling of 1.25 Å pix^{-1}. The WFM, used for the GO data, is 59.9" × 60.0" for each pointing with a spatial pixel scale of 0.2" pix^{-1}. On the other hand, the NFM, used for part of the GTO data, is 7.5" × 7.5" with a spatial pixel scale equal to 0.025" pix^{-1}. In both the GO and the GTO data, some central pointings take also the advantage of the VLT Adaptive Optics Facility (AOF; Arsenault et al. 2010; Ströbele et al. 2012): in that case, the Na I doublet is blocked using a filter in the 5800-5970 Å region, causing a gap in most of the spectra belonging to the thesis sample.
While the GTO data were already reduced and analyzed by Kamann et al. (2018) and Pechetti et al. (2023), the GO data reduction and analysis was performed by Nitschai et al. (2023): for the GO data, all the reduction process, e.g. including correction for bias, flat-field and flux calibration, was done via the MUSE data reduction pipeline version 2.8.3 (Weilbacher et al., 2016, 2020), while PampelMUSE[1] (Kamann et al., 2013) was used for the extraction of the individual spectra, coupling the spectra with the HST photometry from Anderson & van der Marel (2010), which includes data in the F435W and F625W bands of ACS/WFC. By doing this, PampelMUSE was able to fit the Point Spread Function (PSF) as a function of wavelength for all the stars in the catalog, making it possible to separate sources efficiently even in the most crowded regions. After this, all the spectra were fitted via the spectral fitting routine spexxy[2] version 2.5, which compared the observed spectra with synthetic ones, taken from the Phoenix library (Husser et al., 2013), in order to derive the atmospheric parameters - metallicity [M/H], effective temperature T_{eff}, surface gravity log(g) - but also the radial velocity v_{los}, the signal-to-noise ratio S/N and their statistical errors. In particular, the log(g) value was kept fixed in the spectral fitting, at least for RGB stars, as it was first found from the isochrone (taken from the PARSEC

---

[1]https://pampelmuse.readthedocs.io/en/latest/about.html
[2]https://github.com/thusser/spexxy

database, Marigo et al. 2017) that fits the Anderson & van der Marel (2010) photometry. Also, `spexxy` created a fit for the telluric absorption lines, mainly due to H_2O and O_2.

2.1.2 Identification of the discrete populations

The approach used for the identification of the subpopulations consisted in the combination of the HST photometric catalog by Bellini et al. (2017a) (see Sect. 1.2.2) with MUSE spectroscopic metallicities by Nitschai et al. (2023) and will be published in detail in a paper (Clontz et al., in prep.).

Previous papers already identified the distinct stellar populations of ω Cen by using multi-band HST photometry. However, these works were focused on MS stars (Bellini et al., 2017b) and RGB stars (Milone et al., 2017) alone (see Sect. 1.2.2). This work takes the advantage of the synergy between the stellar metallicities, inferred from MUSE spectra, and multi-band HST photometry to disentangle the stellar populations along the entire CMD for the first time, by following the next steps:

❶ **Correction for atomic diffusion (ADC):** it was included in the metallicities because this effect alters the observed metallicities of stars near the MS turnoff (MSTO) in the CMD. The ADC correction includes several internal transport processes as gravitational settling of heavier elements, thermal diffusion, radiative acceleration and turbulent mixing (Nitschai et al., 2023; VandenBerg et al., 2002); these effects cause an offset in metallicity as the stars evolve through the MSTO and enter the SGB, and therefore taking into account the ADC allowed to group the stars by their birth metallicity rather than by the observed atmospheric one.

❷ **Application of the Bayesian Information Criteria (BIC) to find the optimal number of populations**.
The procedure started from a CMD with magnitudes in F814W versus F275W − F814W: first, the reddest population (i.e. the one on the right) was separated from all the others by eye.

After this, a Gaussian mixture model was applied on five magnitude bins of increasing size, starting from $15.5 < m_{F814W} < 15.6$ up to $15.5 < m_{F814W} < 16.0$. The model tested a number of clusters from 1 to 21, using four dimensions: $\Delta_{F275W-F438W}, \Delta_{F275W-F814W}$, the pseudo-color $\Delta C_{F275W,F336W,F438W}$ and the ADC corrected spectroscopic metallicity [M/H], where the color dimension Δ_{X-Y} indicates the difference between the magnitude values and the median color of the correspondent magnitude bin, while the pseudo-color is simply a combination of magnitudes in three different filters, $\Delta C_{F275W,F336W,F438W} = (m_{F275W} - m_{F336W}) - (m_{F336W} - m_{F438W})$. The optimal number of clusters was taken as the median of the lowest values obtained by applying the BIC to the magnitude bins, plus the
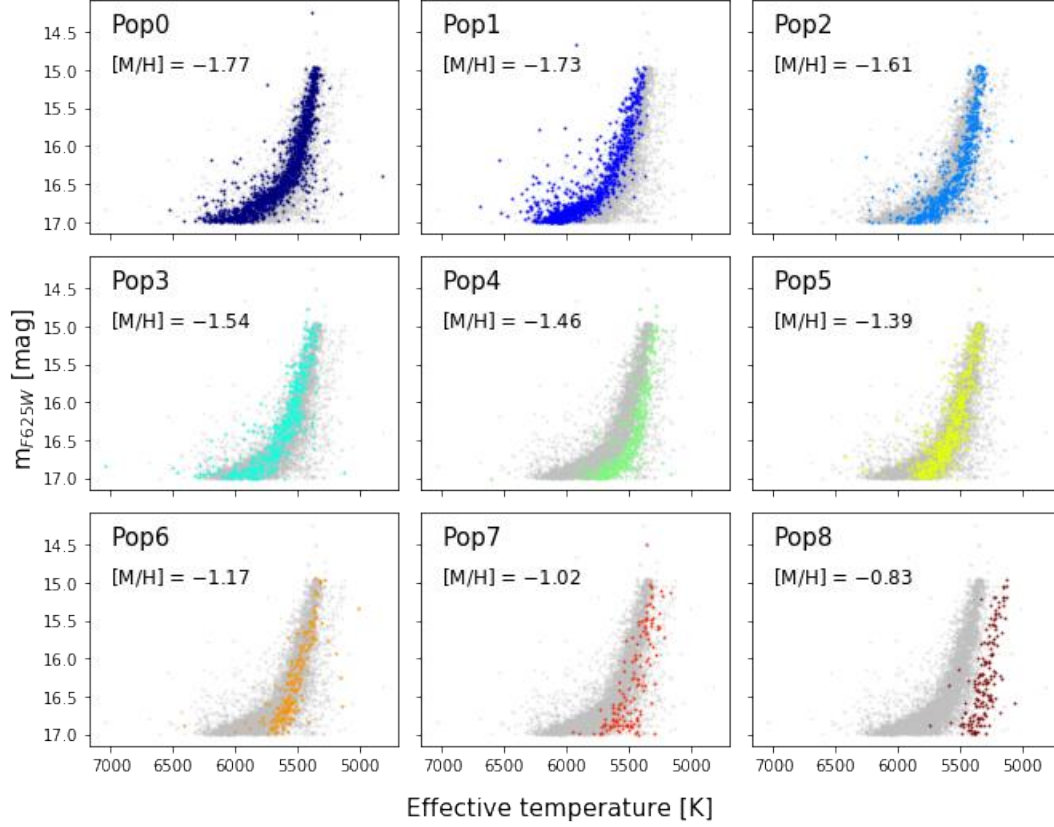
Figure 2.3: Diagrams of magnitude in the F625W filter versus effective temperature of the different stellar populations that were identified from HST photometry, where [M/H] indicates the mean metallicity corrected for atomic diffusion. From Pop0 to Pop8, metallicity increases.

previously isolated reddest cluster. This gave 9 as a final result. The populations were thus labeled as "PopX", with X that ranges from 0 to 8, in order of increasing metallicity.

❸ **Application of the K-Means clustering to bright stars on the RGB.**
The stars with $15.5 < m_{\mathrm{F814W}} < 16$ were selected as a starting point. A K-means clustering was applied to this sample, considering the optimal number of clusters that was previously derived. These bright stars were also used as a training set to find the optimal number of neighbor stars (set at least as five) used in the following point.

❹ **Extension to fainter and brighter stars by using the K-Nearest Neighbor (KNN) algorithm.**

19

This step was developed as a sliding binning process, to include in the analysis also the other stars at higher and lower magnitudes. Starting from the initial sample of bright stars, the process was shifted to fainter stars in fainter magnitude bins with a pace of 0.1 magnitudes. Each time, a KNN was applied using the training set of the previous bin. This algorithm was needed to label the stars and assign them to the correspondent population: it searched the five nearest labeled ones and computed a weighted average to determine the most likely label to be assigned. The process of sliding binning and KNN application was stopped at $m_{\mathrm{F814W}} = 20.2$, and then reiterated to stars brighter than the initial sample, up to $m_{\mathrm{F814W}} = 14.5$.

❺ **Magnitude cut in the F625W filter:** a magnitude cut at $m_{\mathrm{F625W}} = 17$ is applied in order to limit the analysis of this thesis to RGB stars only. The stellar magnitudes in the F625W band are taken from Anderson & van der Marel (2010) and are corrected for extinction and reddening.

In other words, rather than combining the previous disentanglement available from the literature, the MPs were separated by an approach that combines different colors plus the metallicity information. Obviously, the ChMs, that can be effectively built for stars in the RGB and in the MS, were a useful tool that helped parsing the populations. After these were identified, it was possible to perform a preliminary isochrone interpolation taking the models from the Dartmouth grid[3] by Dotter et al. (2008): the best fits allowed to give an estimate of the ages and metallicities for each of the identified populations.

Pop	N
Pop0	1551
Pop1	1076
Pop2	604
Pop3	557
Pop4	395
Pop5	581
Pop6	213
Pop7	139
Pop8	162

Table 2.1: Table reporting the number N of stars for each subpopulation in the thesis sample.

In brief, the considered sample contains 9 stellar populations in total and includes a magnitude cut such that just the brightest stars, i.e. the RGB, are analyzed in the thesis. This choice is made in order to take into account just the stars with lower uncertainties on the metallicity.

---

[3]http://stellar.dartmouth.edu/models/index.html

After matching the clustering catalog with the MUSE spectral catalog, it is possible to visualize the coordinates of the subpopulations belonging to the thesis sample (Fig. 2.2) and their position on the CMD (Fig. 2.3). Their mean metallicities, corrected for atomic diffusion, and the associated errors are estimated in the next Sect. 3.2, while Table 2.1 shows the number of stars in each subpopulation. Moreover, the distributions of their atmospheric parameters are reported in Fig. 2.4 (the metallicity), 2.5 (effective temperature) and 2.6 (surface gravity).
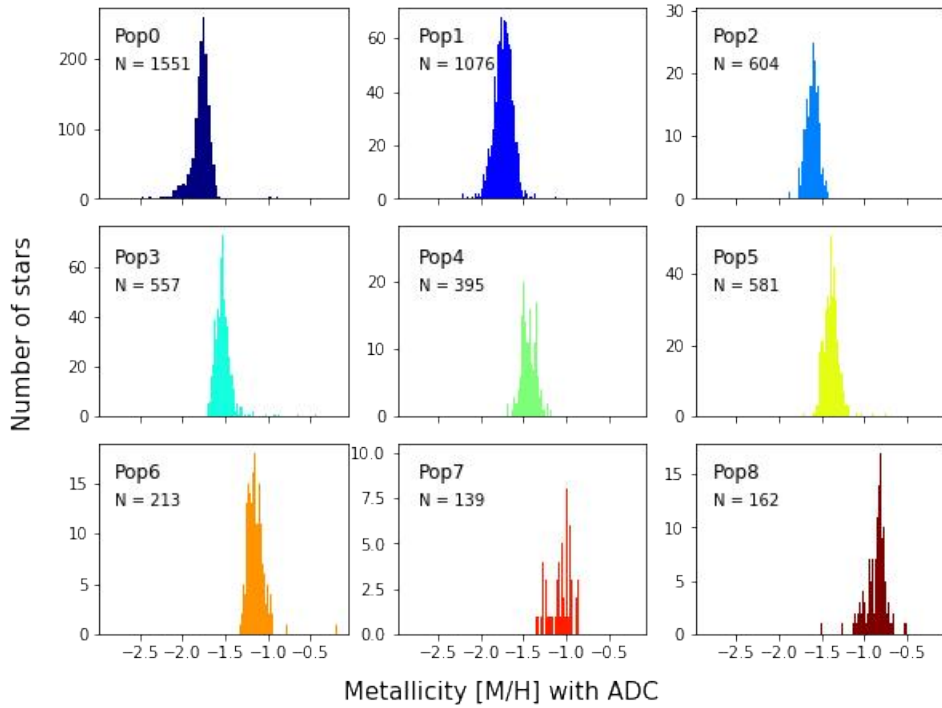
Figure 2.4: Histograms representing the distribution of metallicities, corrected for atomic diffusion, for each of the nine populations. The total number of stars N per population (before the quality cut on S/N, see Sect. 2.2) is reported as well.
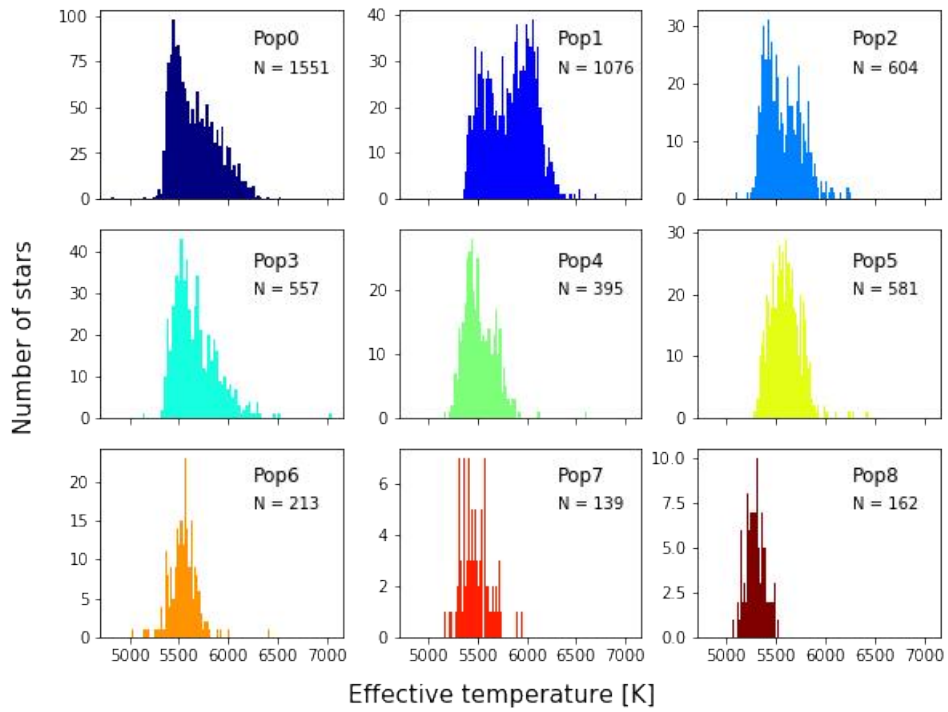
Figure 2.5: Histograms representing the distribution of effective temperature for each of the nine populations. The total number of stars N per population (before the quality cut on S/N, see Sect. 2.2) is reported as well.
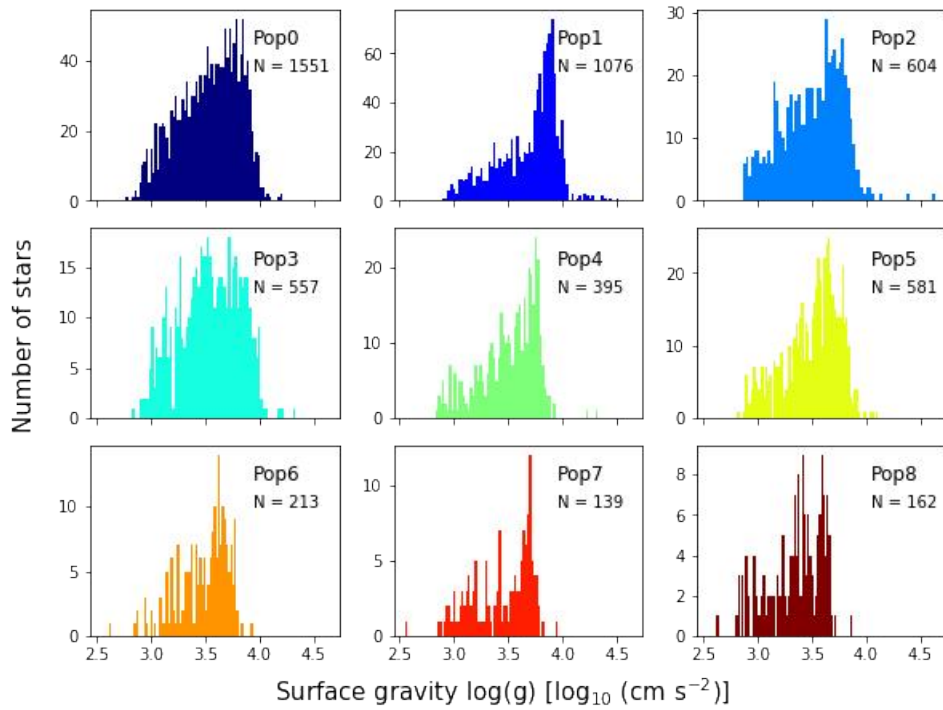
Figure 2.6: Histograms representing the distribution of surface gravity for each of the nine populations. The total number of stars N per population (before the quality cut on S/N, see Sect. 2.2) is reported as well.

2.2 Individual spectra

After the spectral data reduction, the individual spectra can be visualized as `fits` files with the `QFitsView` software. Each of these files contains a raw spectrum (Fig. 2.7, *top*) and other elements useful to remove the telluric lines and optimize the continuum level: in particular, the telluric spectral model and the `multpoly`, which is a polynomial representing the difference between the observed spectrum and the model (i.e. similar to a continuum if the model was normalized). For the thesis work, only spectra with signal-to-noise ratio S/N > 10 are considered.
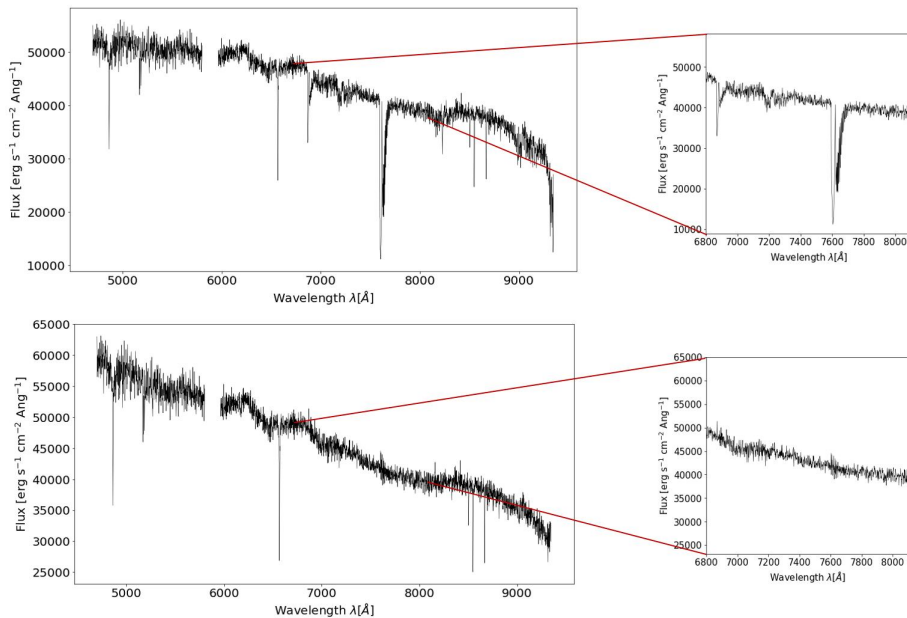

Figure 2.7: *Top*: raw spectrum as an example of the initial individual spectra that came from the spectral extraction and fitting procedure, with a zoom in on the main telluric absorption lines. *Bottom*: an example of raw spectrum corrected by tellurics; the absorption lines due to the atmospheric absorption disappear.

The correction for telluric lines is the first step needed. In fact, as the spectra are taken from Earth, they suffer from the contamination of the absorption lines of the atmosphere - mainly H_2O and O_2 - which can effectively be removed dividing each spectra by the telluric model. An example of raw spectrum, corrected by tellurics, is reported in Fig. 2.7, *bottom*.
After this, the next operation is to divide each spectrum by the correspondent `multpoly`

so as to get rid of the uneven continuum: the spectrum looks then straighter, as the example reported in Fig. 2.8.
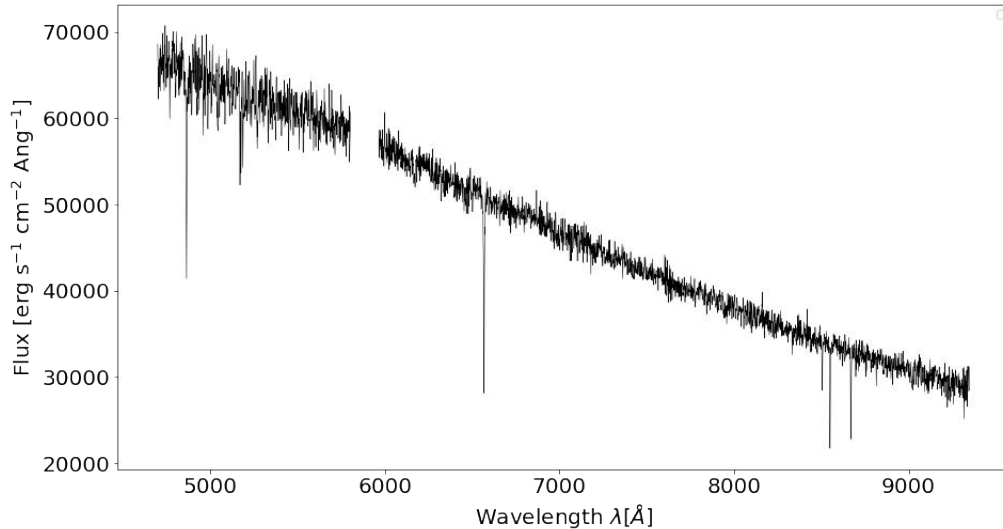

Figure 2.8: An example of individual spectrum after both tellurics and `multpoly` correction. The gap in the Na I doublet region is clearly visible.

Then, a wavelength calibration is performed, in order to move from pixel units to units of wavelength λ. To shift all the lines to their rest-frame, the redshift correction is needed as well, but in GO data only - the GTO data contain this correction already. The equation for the Doppler effect, holding in case of low cosmological redshift ($z << 1$), is:

$$\lambda_0 = \frac{\lambda}{1 + v_{\text{los}}/c} \tag{2.1}$$

where λ_0 is the rest frame wavelength, λ is the observed wavelength, $c \simeq 299792$ km/s is the speed of light and v_{los} is the radial velocity (the component along the line of sight) that comes from the spectral data reduction.

After all the lines are successfully shifted to their rest frame, it is possible to identify them taking the rest frame wavelengths from the `NIST` database[4]. Even if the most prominent lines are already clearly visible from the individual spectrum, a proper identification is made after the stacking, when also the weakest ones can be recognized.

Because of the AO gap (see Sect. 2.1.1), most of the spectra lack the flux values in the region between 5800-5970 Å. Therefore, to avoid making an uneven statistics by mixing spectra that show the gap with the few that don't, a masking in the 5780-5990 Å window is included, unfortunately preventing the Na I sodium doublet from being analyzed.

---

[4]https://physics.nist.gov/PhysRefData/ASD/lines_form.html

2.3 Preparation of the stacked spectra

The idea of spectral stacking is to create a spectrum that is representative of a single population (Latour et al., 2019). In this sense, hundreds or even thousands of low resolution MUSE stellar spectra are combined in a single one, increasing the S/N and making it possible to investigate the abundance variations among the populations, despite the low S/N of the initial individual spectra.

Since this technique (further explained in Sect. 3.1) intends to create an average spectrum, all the individual spectra of each single population must be summed in the process: to do this, they must start and end at the same wavelength value and, in general, be resampled to the same wavelength grid. To avoid possible systematic errors due to the comparison of stars in very different evolutionary stages, four stacked spectra for each population are generated, in such a way that each spectrum comprises stars in different magnitude bins (Sect. 3.1.1).

First, the edges of all the individual spectra are cut of an amount of ~ 50 Å. This is needed also to remove possible outlier values in the flux, which are sometimes located at the start and at the end of the spectra, possibly after the spectral extraction. At this point, all the spectra are resampled to the same wavelength grid by a binning operation, performed by using the `SpectRes`[5] Python package by Carnall (2017): the chosen bin size is 1.25 Å, i.e. equal to the instrumental resolution, so as not to undersample nor oversample the flux data. What `SpectRes` does is generally to resample spectral flux densities onto different wavelengths grids, and it works with any initial grid of wavelength values, also non-uniform samplings, preserving the integrated flux.

After this operation, the individual spectra are ready to be stacked.

---

[5]https://spectres.readthedocs.io/en/latest/

Data analysis

3.1 Stacked spectra

To infer the abundances of the stellar populations of ω Cen, the method introduced by Latour et al. (2019) in their study of RGB stars of NGC 2808 is applied. In a nutshell, four magnitude intervals are considered and, for each of them, the spectra of all stars in each stellar population of ω Cen are combined. The outcome is a high S/N stacked spectrum that is representative of the whole population.

To account for the signal-to-noise ratio (S/N) of the individual spectra, a weighted average is performed, by setting the S/N as the weight, and normalizing the flux of the stacked spectra to the sum of the weights. In this way, the spectra with lower S/N affect less the final result, and also the contribution from outlier values in the flux is minimized.

This technique has the following advantages:

- it allows us to infer the abundance variations among the populations, despite the individual spectra have low S/N that could prevent such analysis;

- all spectra, including those that have low S/N ratio (provided that S/N>10), contribute to the analysis;

- the stacked spectrum represents the average chemical behaviour of the set of stars included in the stacking, allowing an immediate comparison of the mean chemical properties among the populations.

Furthermore, the stacked spectra is created not only per subpopulation, but also per magnitude bin all along the RGB, so that each subpopulation is related to four stacked spectra in total that represent it. This choice allows to verify that the resulting chemical compositions don't depend on stellar magnitude.

This chapter is composed of Sect. 3.1.1, which provides details on the procedure to derive the stacked spectra, and Sect. 3.1.2 that mainly focuses on the normalization of the

stacked spectra to the continuum level. Furthermore, Sect. 3.2 includes the determination of the mean metallicities of the nine populations with their associated errors.
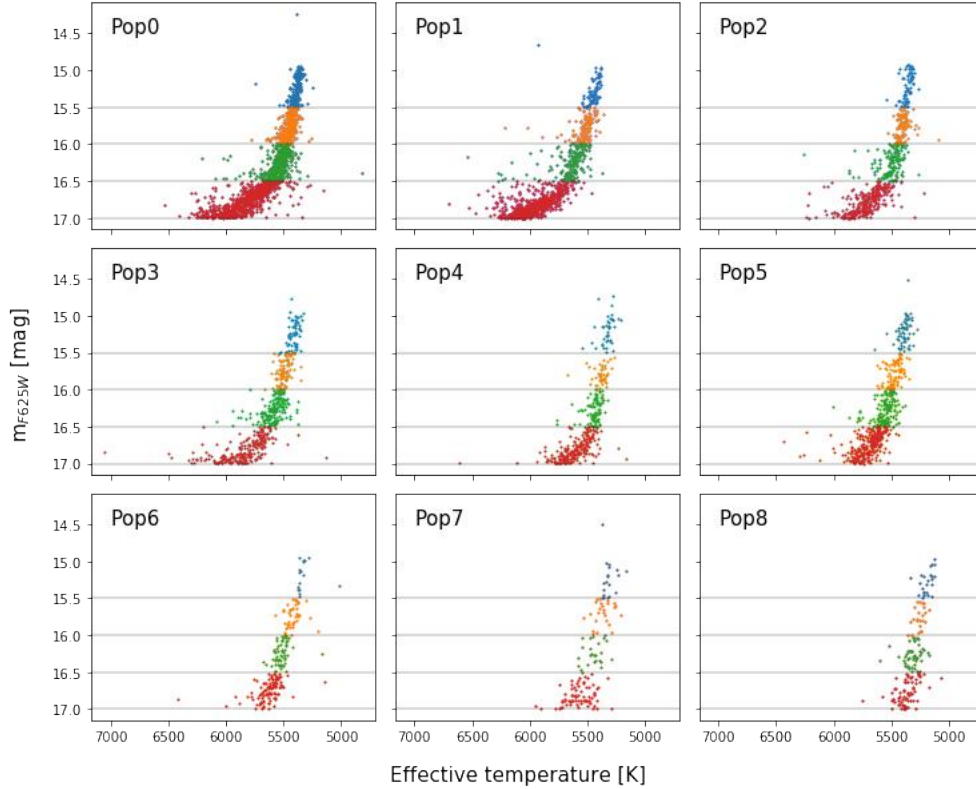

Figure 3.1: CMDs of the nine populations, showing the four magnitude bins. Blue stars belong to Group0 ($m_{F625W} \leq 15.5$), orange stars to Group1 ($15.5 < m_{F625W} \leq 16.0$), green stars are in Group2 ($16.0 < m_{F625W} \leq 16.5$) and red ones in Group3 ($16.5 < m_{F625W} \leq 17.0$).

3.1.1 Magnitude binning

In order to combine stars with more homogeneous atmospheric parameters, the stacking is performed not only per each stellar population, but also per magnitude bin. As a matter of fact, stars in very different evolutionary stages could bring to some systematics in the results. For example, magnitude binning would reduce the effect of line broadening, especially on the wings of the line, caused when surface gravity log(g) and/or effective temperature T_{eff} have large variations among the combined stars.

To do this, it is first possible to visualize the populations in a diagram that has the F625W magnitude (from Anderson & van der Marel 2010) on the y-axis and the effective temperature T_{eff} on the x-axis. Starting from these diagrams, magnitude bins are selected,

leading to the division of stars in four bins, called "Groups" - from Group0, the brightest, to Group3, containing the weakest stars. Each Group spans an interval of 0.5 magnitudes, with the exception of Group0. This choice is due to the small number of stars brighter than m_{F625W}=15.0 mag. Specifically, Group0 hosts stars with $m_{\mathrm{F625W}} \leq 15.5$, whereas Groups 1, 2, and 3 comprise stars with $15.5 < m_{\mathrm{F625W}} \leq 16.0$, $16.0 < m_{\mathrm{F625W}} \leq 16.5$, and $16.5 < m_{\mathrm{F625W}} \leq 17.0$, respectively.

The magnitude binning done on the diagrams is reported in Fig. 3.1. A stacked spectrum is then created for each Group, so that four spectra are available for each population.

The stacking process consists in using the individual spectra - that result from the reduction in Sect. 2.3 - with their correspondent value of S/N to compute a weighted average of the fluxes per each wavelength value. This computation uses the S/N as weight and takes into account the number of stars as well.

Table 3.1 reports the number of stars for a specific Group and subpopulation and the total number of stars N_{tot} for that subpopulation, which can be slightly different to the number indicated in Sect. 2.1.2 due to the cut that is applied on the S/N.

PopX	Group0	Group1	Group2	Group3	N_{tot}
Pop0	162	264	375	744	1545
Pop1	73	118	182	702	1075
Pop2	69	106	141	285	601
Pop3	58	98	167	229	552
Pop4	41	44	91	218	394
Pop5	63	89	150	275	577
Pop6	16	41	55	101	213
Pop7	19	25	25	69	138
Pop8	23	23	47	68	161

Table 3.1: Number of stars belonging to each specific Group and subpopulation. The Table provides also the total number of stars N_{tot} that are used to derive the stacked spectra per each population and Group.

3.1.2 Normalization of the stacked spectra

Once the stacking is complete, the resulting spectra are normalized to the continuum in order to make the comparison more straightforward. This operation is done by using the `specutils`[1] Python package, which fits the continuum with the `fit_generic_continuum` function. In doing this, the windows where the absorption lines lie are specified and excluded from the fitting process: the better the line identification, the better the continuum

---

[1]https://specutils.readthedocs.io/en/stable/

fit.

The stacked spectra and their normalization are reported in Fig. 3.2, 3.3, 3.4, 3.5, 3.6, 3.7, 3.8, 3.9, 3.10, where the black line indicates the continuum fit performed by `specutils`. In order to highlight the improvement given by spectral stacking, one of the individual spectra of Pop6 is normalized as well and shown in Fig. 3.11, while its stacked counterpart (Pop6, Group0) is reported in Fig. 3.12, with a zoom in on the 7640-7720 Å window.
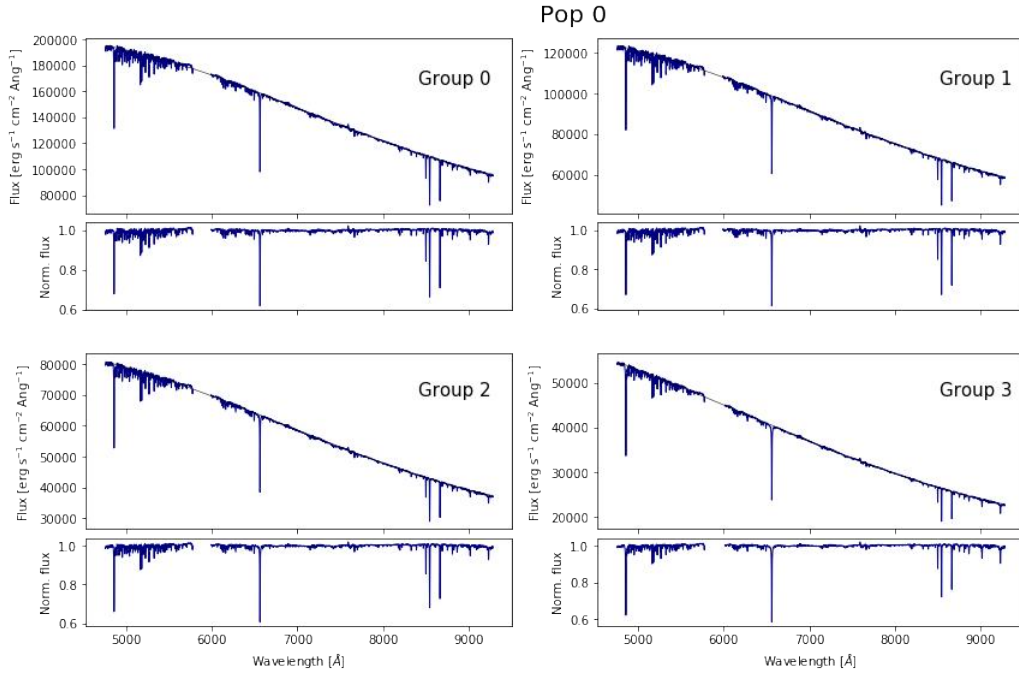

Figure 3.2: Stacked spectra of Pop0 before and after normalization.
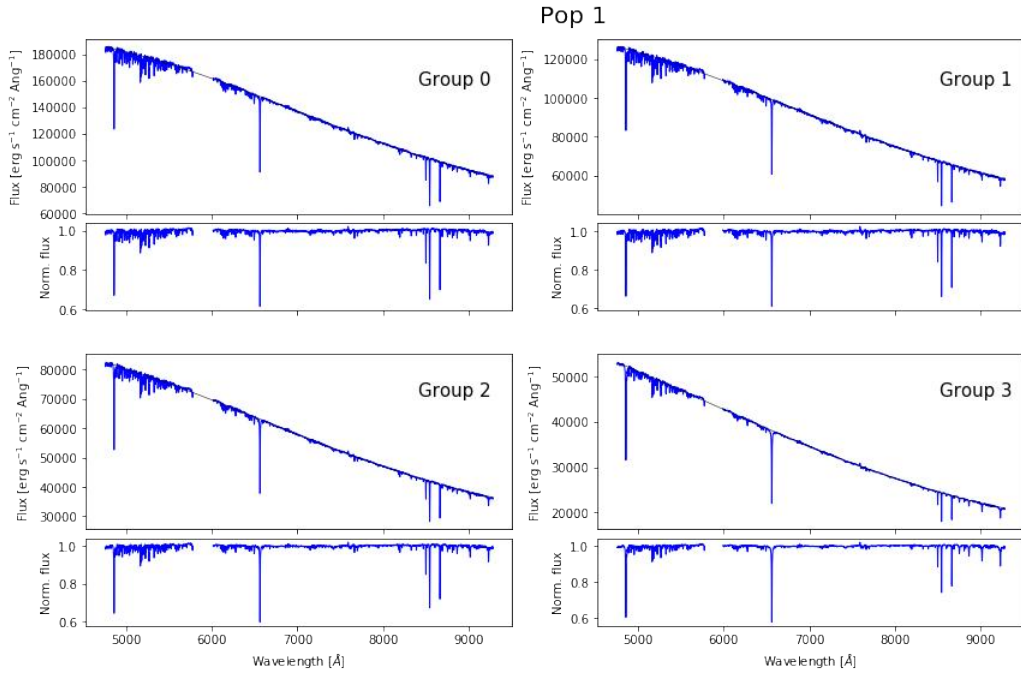
Figure 3.3: Stacked spectra of Pop1 before and after normalization.
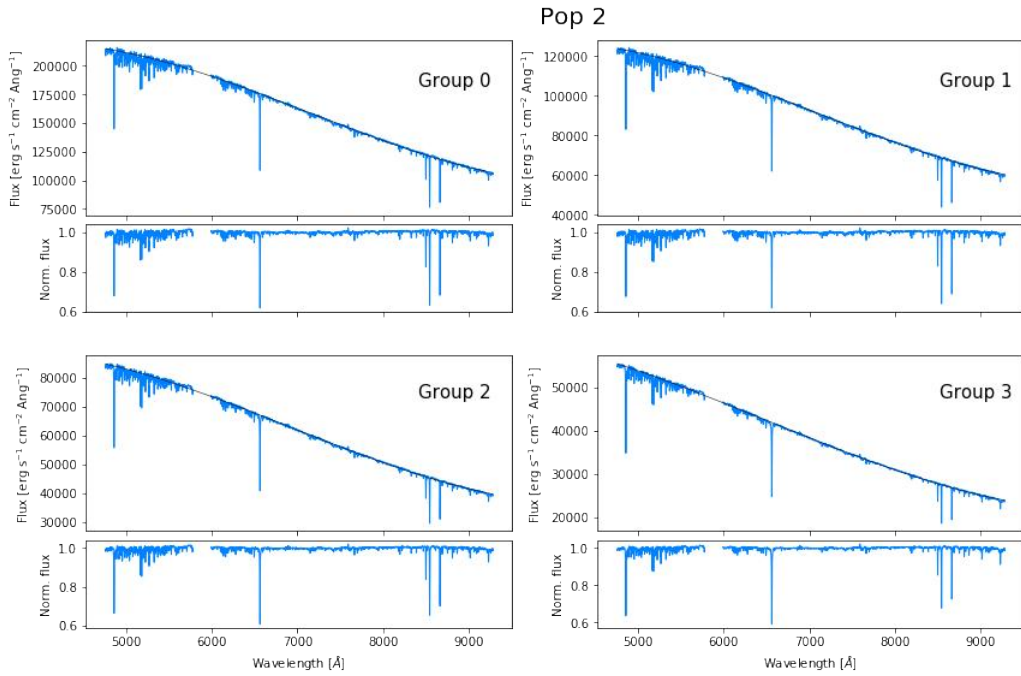
Figure 3.4: Stacked spectra of Pop2 before and after normalization.
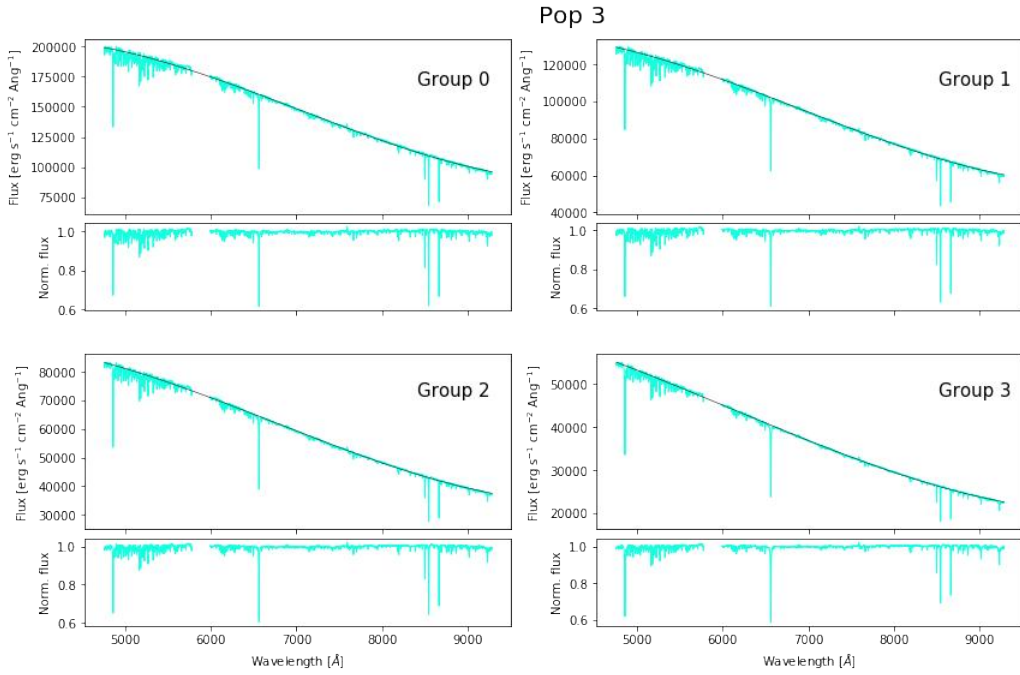
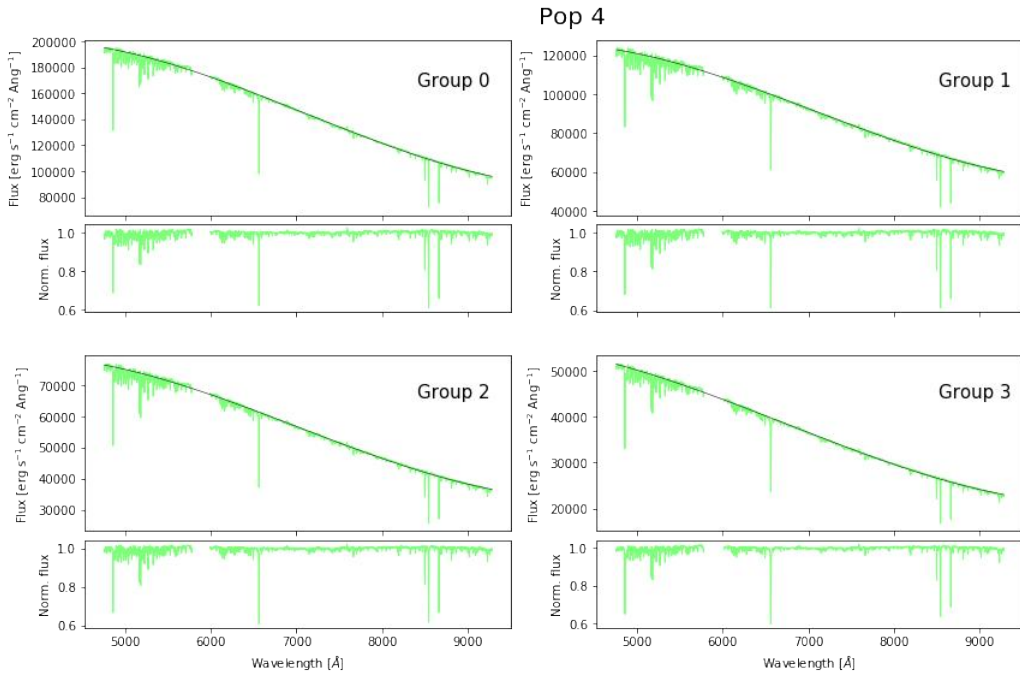Figure 3.5: Stacked spectra of Pop3 before and after normalization.

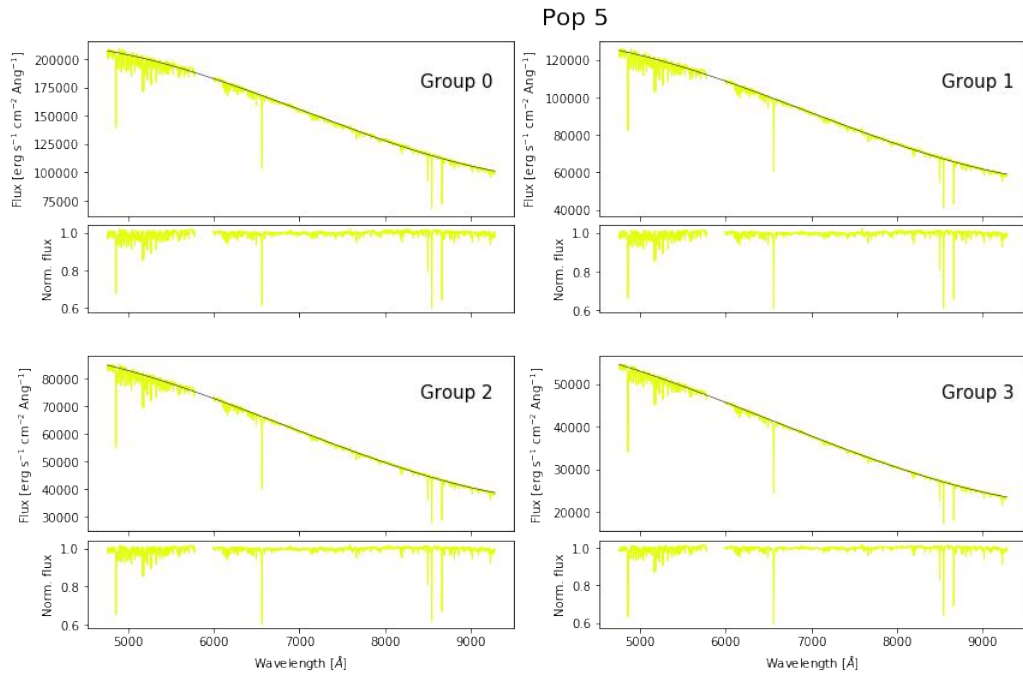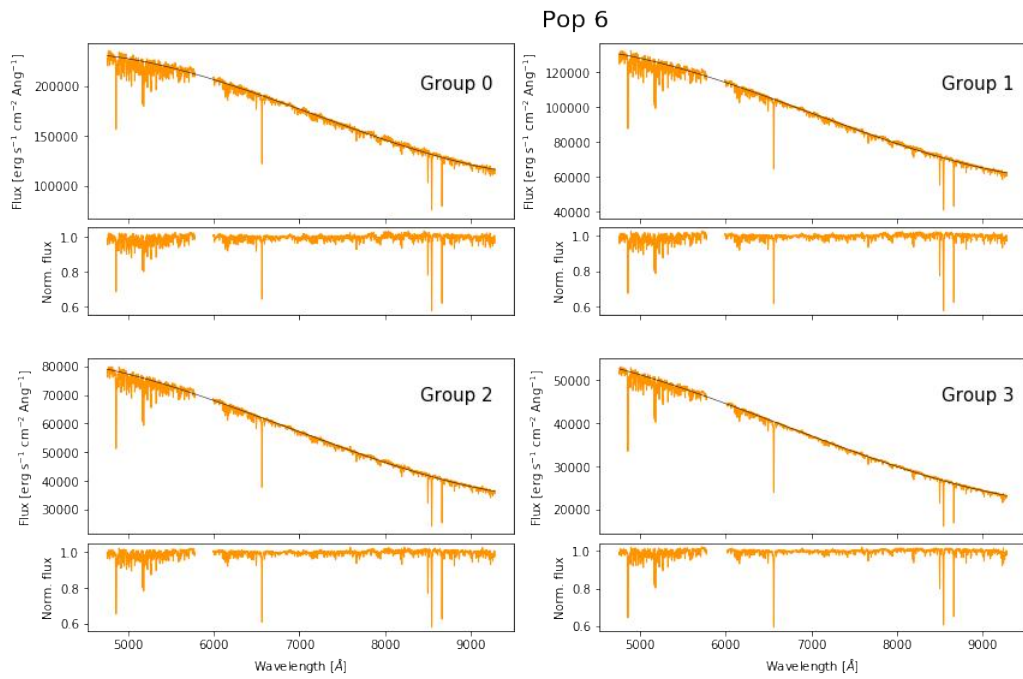Figure 3.6: Stacked spectra of Pop4 before and after normalization.

Figure 3.7: Stacked spectra of Pop5 before and after normalization.

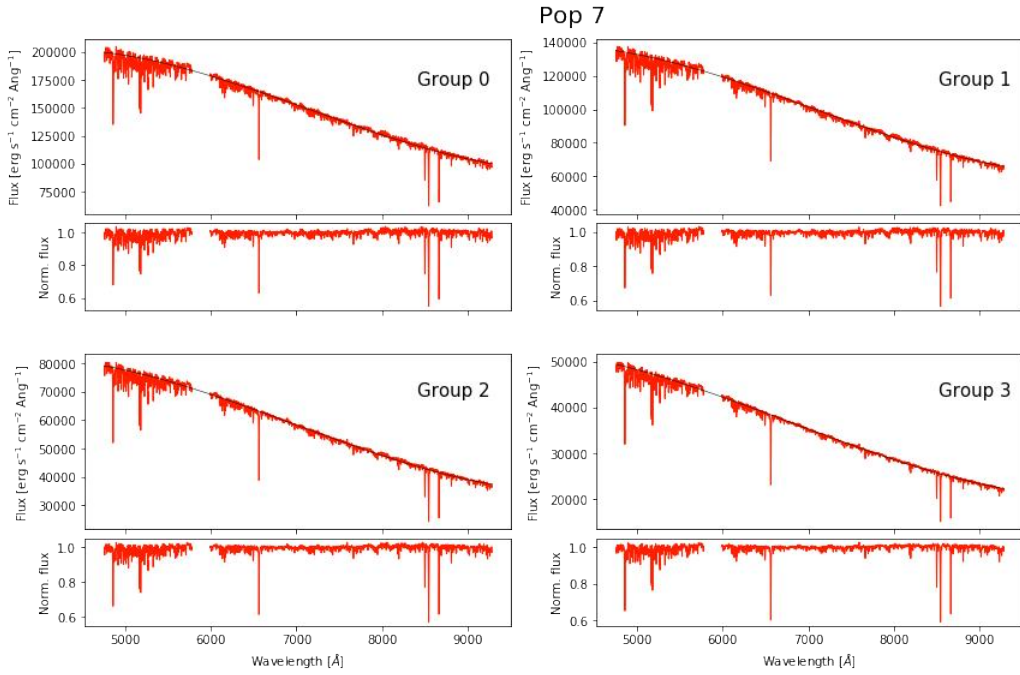Figure 3.8: Stacked spectra of Pop6 before and after normalization.

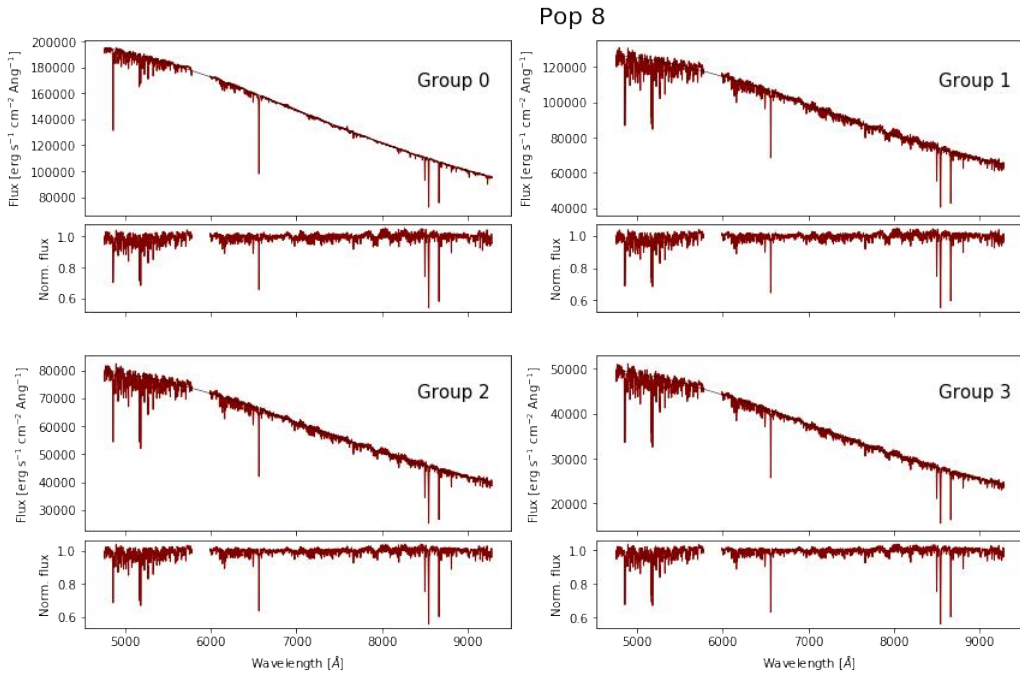Figure 3.9: Stacked spectra of Pop7 before and after normalization.

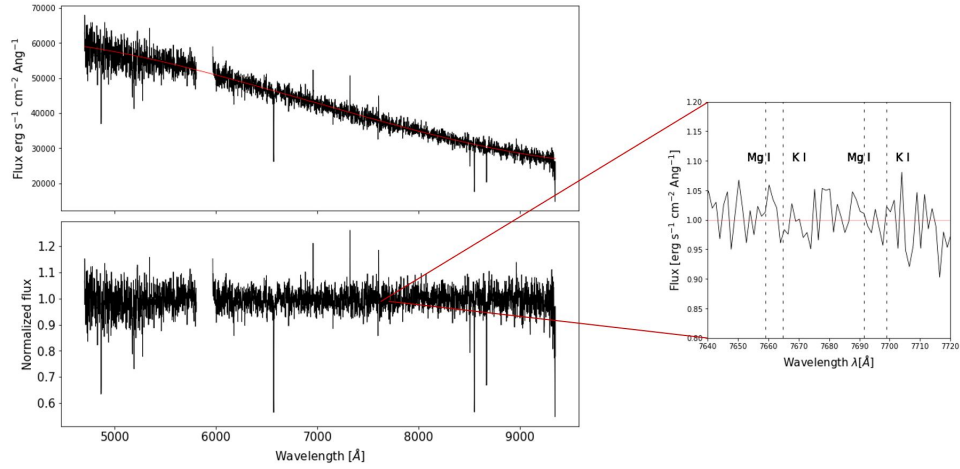Figure 3.10: Stacked spectra of Pop8 before and after normalization.

Figure 3.11: An example of individual spectrum of Pop6: the spectrum is corrected by tellurics, `multpoly` and Doppler redshift and normalized to the continuum - the red line represents the continuum fit. A zoom in on the 7640-7720 Å window is shown: two Mg I and two K I lines should be found here, but the low S/N prevents their identification.
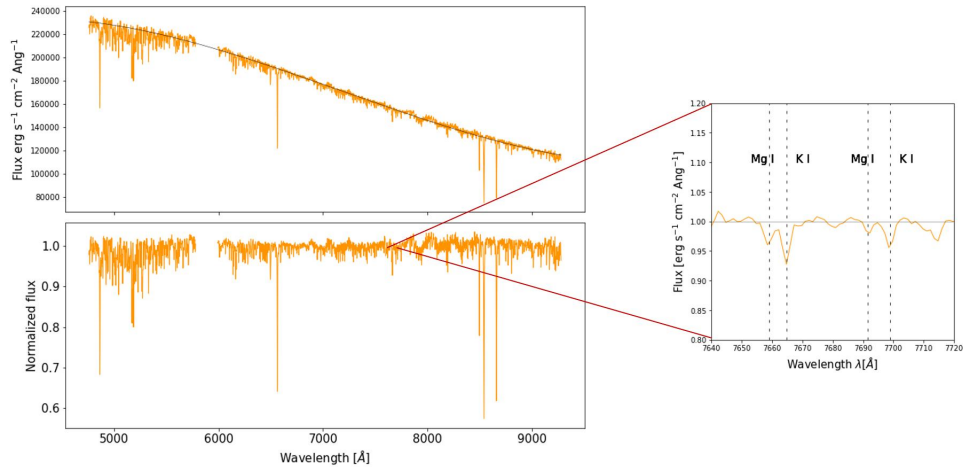

Figure 3.12: The stacked spectrum of Pop6, Group0, already shown in Fig. 3.8, with a particular focus on the 7640-7720 Å region. Two Mg I and two K I lines are now visible, thanks to the increase of S/N that follows the stacking.

3.2 Mean metallicity of the populations

The spectral data reduction (Sect. 2.1.1) provides an estimate of the mean atomic diffusion corrected metallicity for every single star in the thesis sample. In order to give an estimate for the mean metallicity $[M/H]_{\mathrm{Pop}}$ that characterizes each subpopulation and, at the same time, to check that the metallicity of a population does not change with magnitude, the following steps are taken:

❶ a median metallicity $[M/H]_{\mathrm{Group}}$ is calculated for each of the four Groups listed in Sect. 3.1.1 and for each of the nine populations.

❷ for each $[M/H]_{\mathrm{Group}}$, the associated error σ_{Group} is computed as:

$$\sigma_{\mathrm{Group}} = \sqrt{\frac{\sum_i ([M/H]_i - [M/H]_{\mathrm{Group}})^2}{N-1}}$$

where $[M/H]_i$ is the metallicity value of the individual star and N is the total number of stars in the Group.

❸ Each population has now four median values of the metallicity, which are reported in Table 3.2 and which turn out to be consistent with each other.

❹ $[M/H]_{\mathrm{Pop}}$ is calculated as the weighted average of the four $[M/H]_{\mathrm{Group}}$, with an associated error equal to:

$$\sigma_{\mathrm{Pop}} = \sqrt{\frac{1}{\sum_i 1/\sigma_{\mathrm{Group,i}}^2}}$$

These values are all reported in Table 3.2 as well.

Pop	Group	$[\mathrm{M/H}]_{\mathrm{Group}} \pm \sigma_{\mathrm{Group}}$	$[\mathrm{M/H}]_{\mathrm{Pop}} \pm \sigma_{\mathrm{Pop}}$
Pop0	Group0	-1.77 ± 0.05	-1.77 ± 0.04
	Group1	-1.76 ± 0.08	
	Group2	-1.77 ± 0.15	
	Group3	-1.78 ± 0.17	
Pop1	Group0	-1.74 ± 0.07	-1.73 ± 0.04
	Group1	-1.72 ± 0.08	
	Group2	-1.71 ± 0.11	
	Group3	-1.75 ± 0.12	
Pop2	Group0	-1.63 ± 0.05	-1.61 ± 0.03
	Group1	-1.62 ± 0.05	
	Group2	-1.61 ± 0.06	
	Group3	-1.58 ± 0.08	
Pop3	Group0	-1.55 ± 0.05	-1.54 ± 0.03
	Group1	-1.54 ± 0.06	
	Group2	-1.52 ± 0.08	
	Group3	-1.53 ± 0.15	
Pop4	Group0	-1.48 ± 0.08	-1.46 ± 0.04
	Group1	-1.46 ± 0.09	
	Group2	-1.44 ± 0.07	
	Group3	-1.44 ± 0.09	
Pop5	Group0	-1.39 ± 0.07	-1.39 ± 0.04
	Group1	-1.39 ± 0.10	
	Group2	-1.39 ± 0.10	
	Group3	-1.40 ± 0.09	
Pop6	Group0	-1.18 ± 0.15	-1.17 ± 0.05
	Group1	-1.15 ± 0.10	
	Group2	-1.11 ± 0.15	
	Group3	-1.19 ± 0.08	
Pop7	Group0	-0.99 ± 0.08	-1.02 ± 0.05
	Group1	-1.02 ± 0.11	
	Group2	-1.01 ± 0.15	
	Group3	-1.07 ± 0.13	
Pop8	Group0	-0.83 ± 0.17	-0.83 ± 0.06
	Group1	-0.83 ± 0.11	
	Group2	-0.84 ± 0.10	
	Group3	-0.83 ± 0.14	

Table 3.2: Table reporting the median metallicity $[\mathrm{M/H}]_{\mathrm{Group}}$ per magnitude bin, with the corresponding error σ_{Group}. Also the weighted average of these four $[\mathrm{M/H}]_{\mathrm{Group}}$ is reported, for each subpopulation, with its associated error σ_{Pop}.

Discussion and conclusions

4.1 Qualitative comparison of the stacked spectra

The stacked spectra that are derived in Sect. 3.1.2 can be compared to each other. In the following, the same Groups of different subpopulations are plotted together, and the most prominent lines are zoomed in:

- Hβ (4861.31 Å) and a Ba II line (4934.08 Å) in Fig. 4.1;

- Mg I triplet (MgT at 5167.32 Å, 5172.70 Å, 5183.60 Å) in Fig. 4.2;

- Hα (6562.80 Å), Al I (6696.01 Å) and another Ba II line (6496.89 Å) in Fig. 4.3;

- a window with two lines of Mg I (7659.12 Å, 7691.55 Å) and two lines of K I (7664.90 Å, 7698.96 Å), in Fig. 4.4;

- two lines of Na I (8183.25 Å, 8194.80 Å) in Fig. 4.5;

- Ca II triplet (CaT at 8498.02 Å, 8542.09 Å, 8662.14 Å) in Fig. 4.6

Black dashed lines indicate the rest wavelengths taken from the NIST database.

On the other hand, Fig. 4.7, 4.8, 4.9, 4.10, 4.11 and 4.12 show the correspondent difference between the normalized fluxes of the populations and the one of Pop0, which is taken as reference.

This Sect. 4.1 provides some qualitative considerations on the chemical properties that can be drawn from these plots. Eventually, Sect. 4.2 defines the future projects that can follow this thesis work.
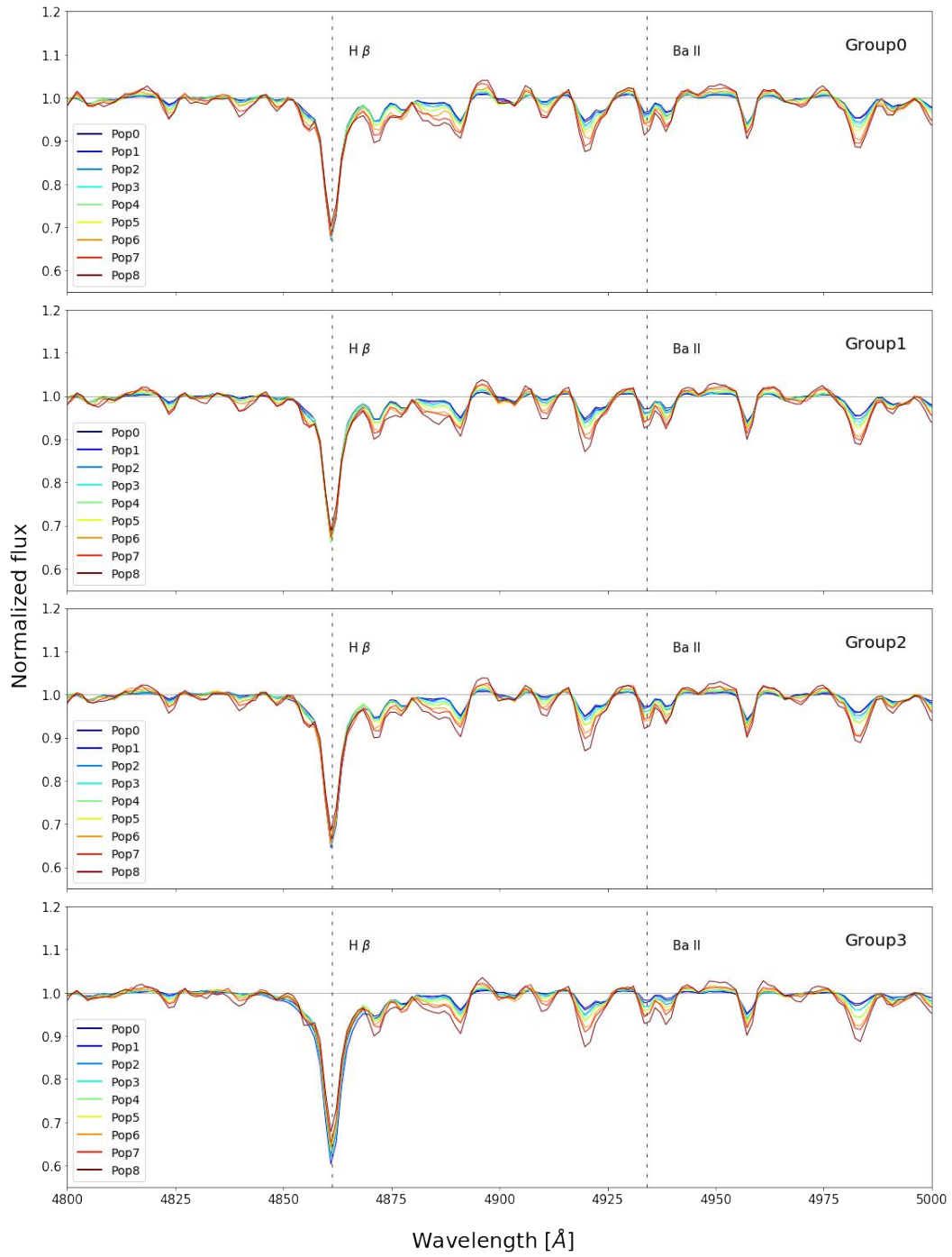
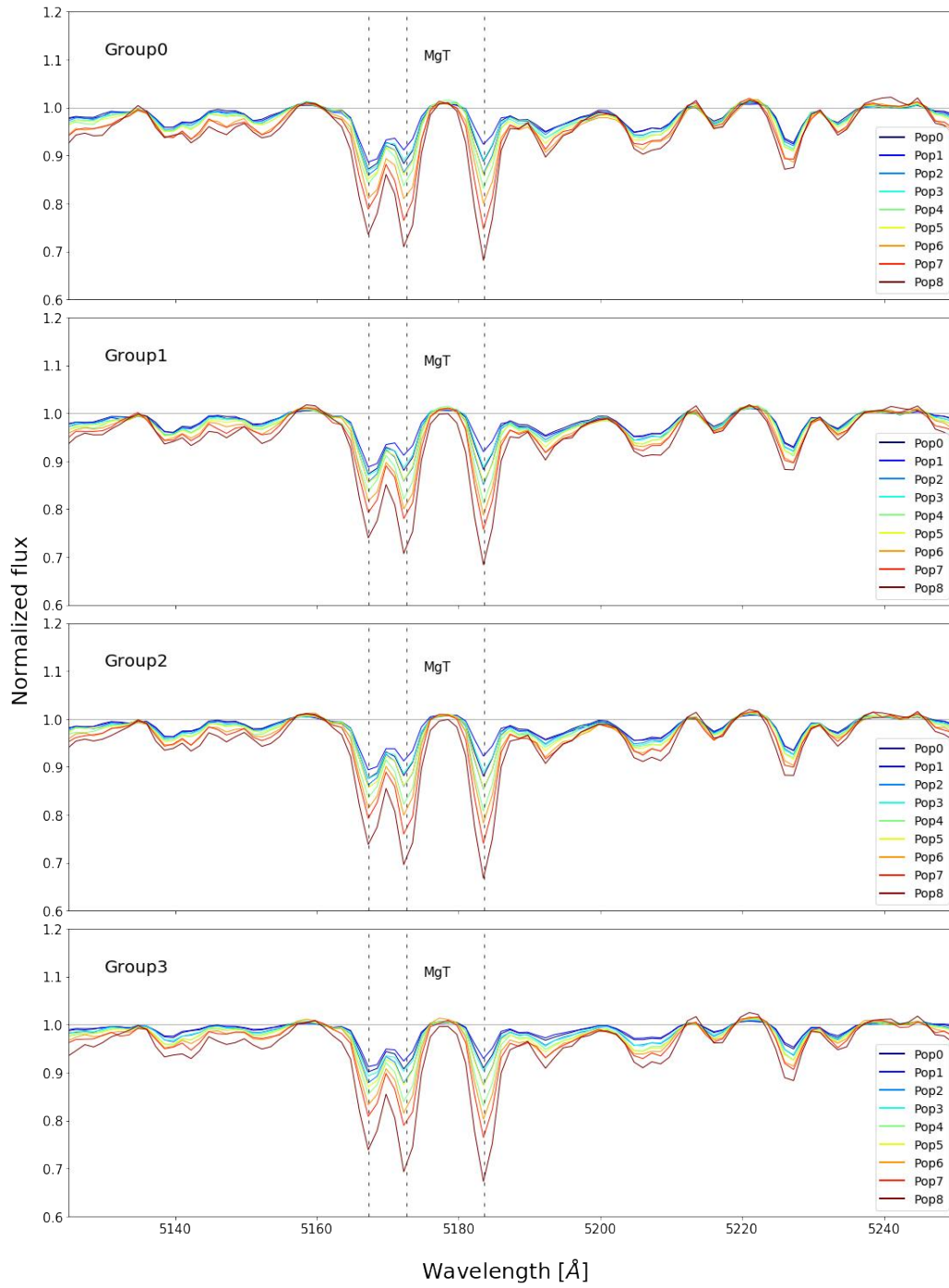Figure 4.1: Hβ and a Ba II line in different Groups and subpopulations.
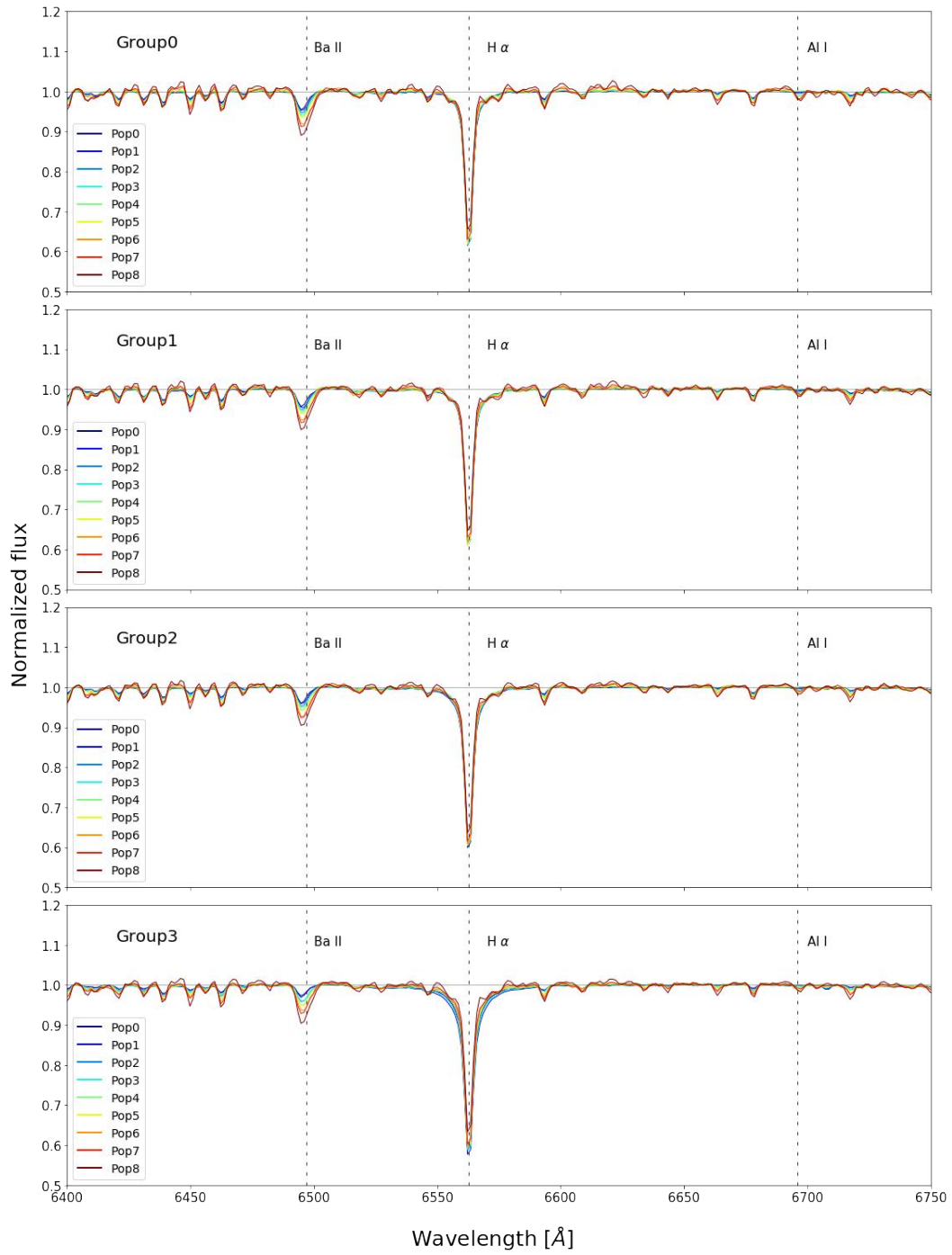
Figure 4.2: MgT in different Groups and subpopulations.

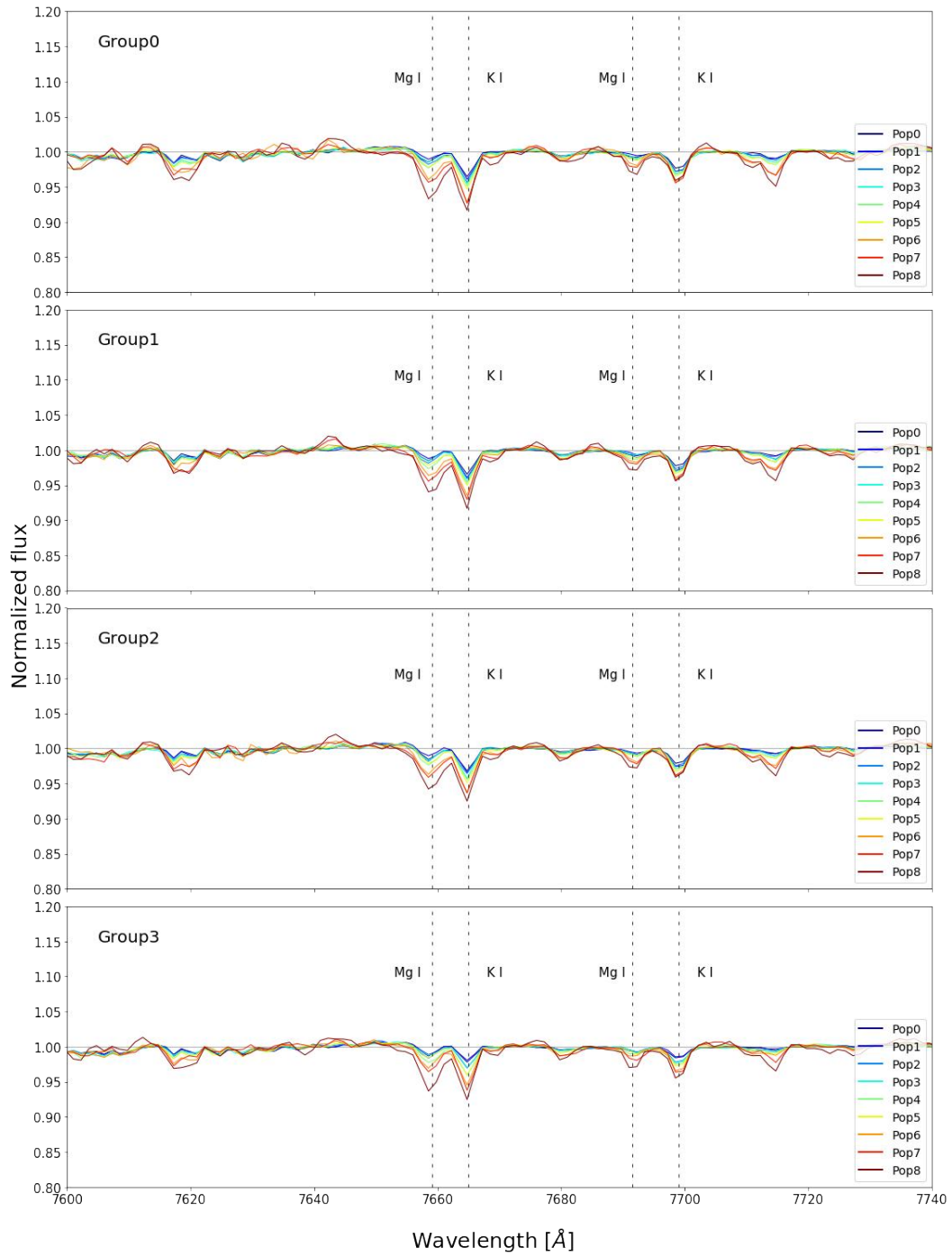Figure 4.3: Hα, Ba II and Al I lines in different Groups and subpopulations.

Figure 4.4: Two Mg I and two K I lines in different Groups and subpopulations.
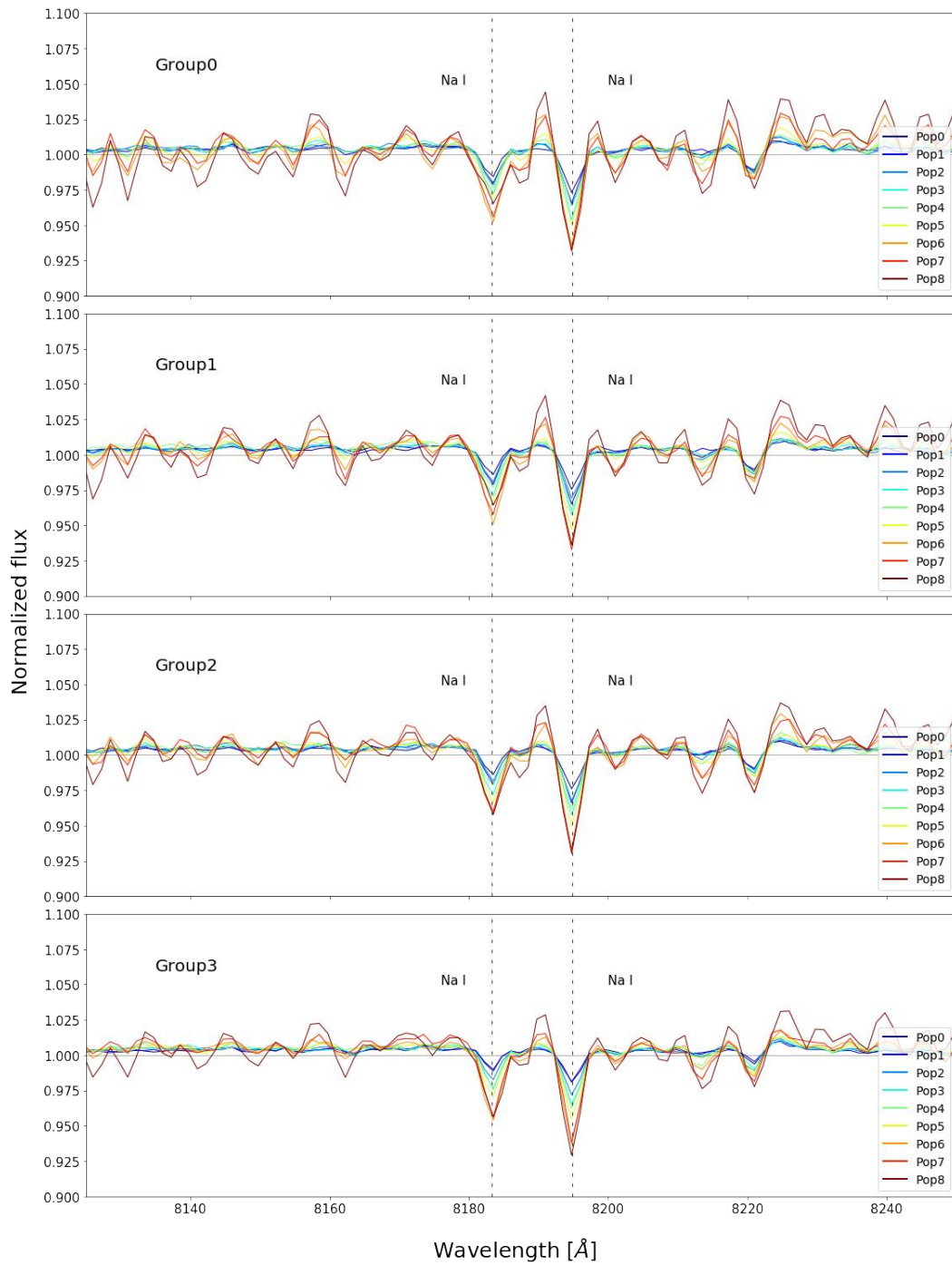
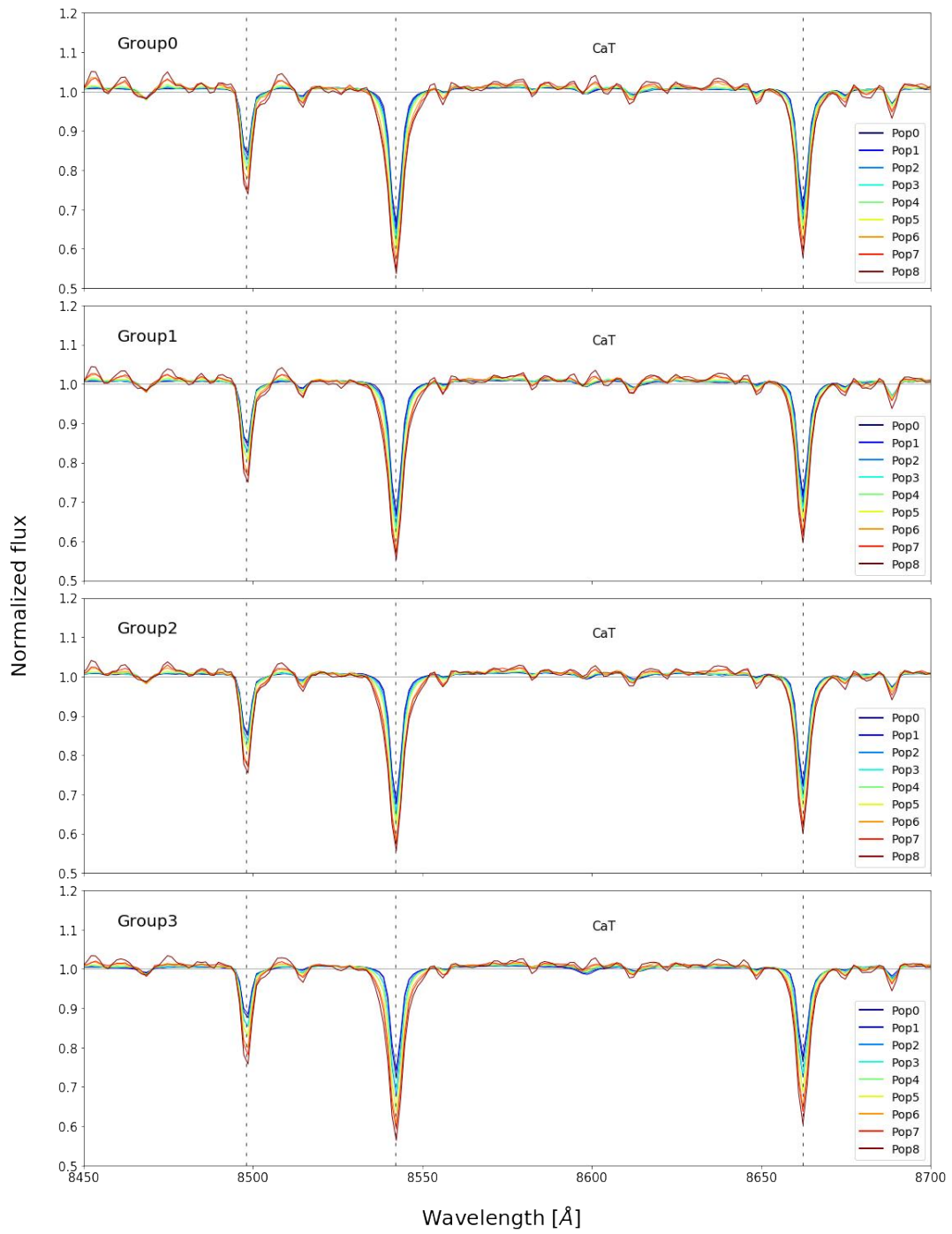Figure 4.5: Two Na I lines in different Groups and subpopulations.

Figure 4.6: CaT in different Groups and subpopulations.
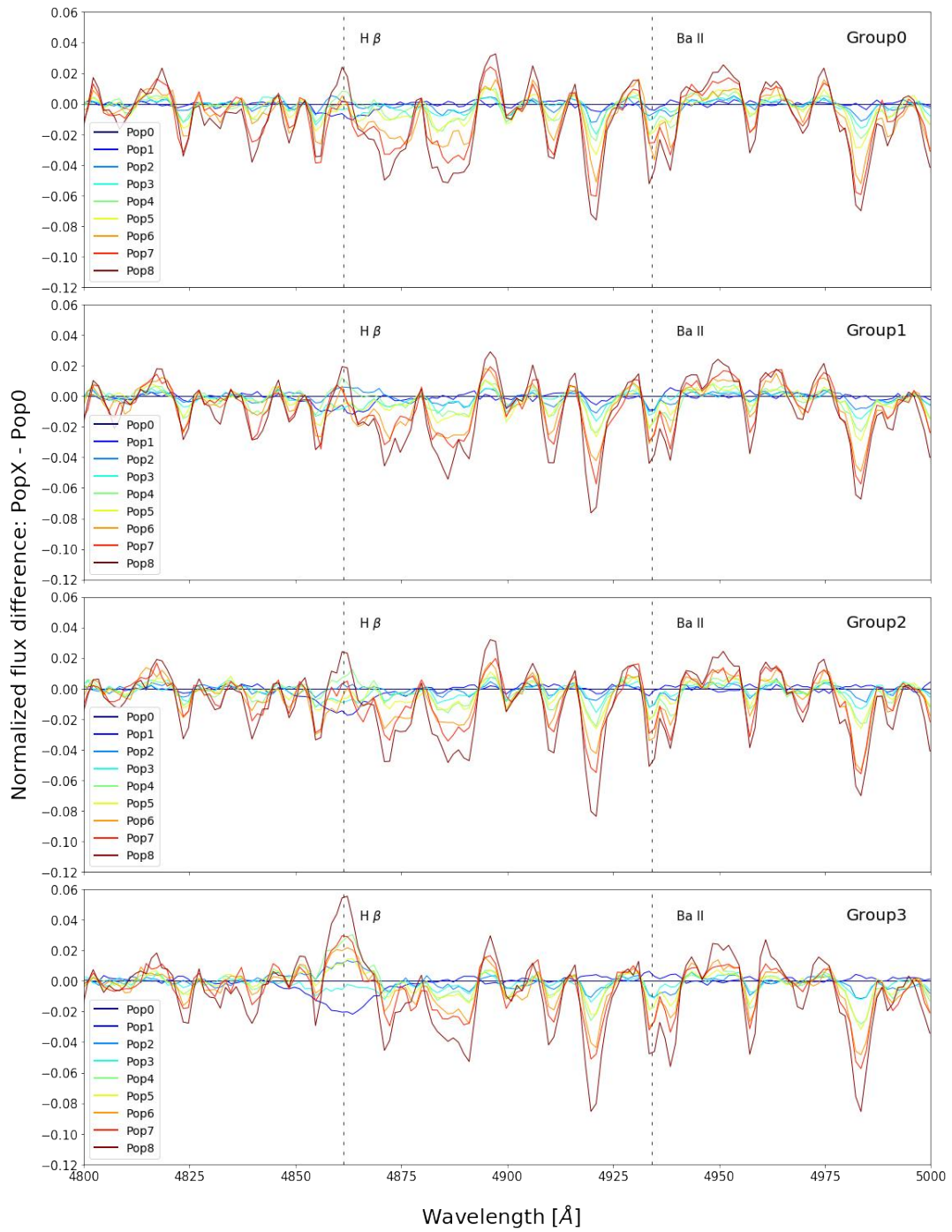
Figure 4.7: Flux difference of each subpopulation with respect to Pop0, in the same wavelength window as Fig. 4.1.

Figure 4.8: Flux difference of each subpopulation with respect to Pop0, in the same wavelength window as Fig. 4.2.

Figure 4.9: Flux difference of each subpopulation with respect to Pop0, in the same wavelength window as Fig. 4.3.
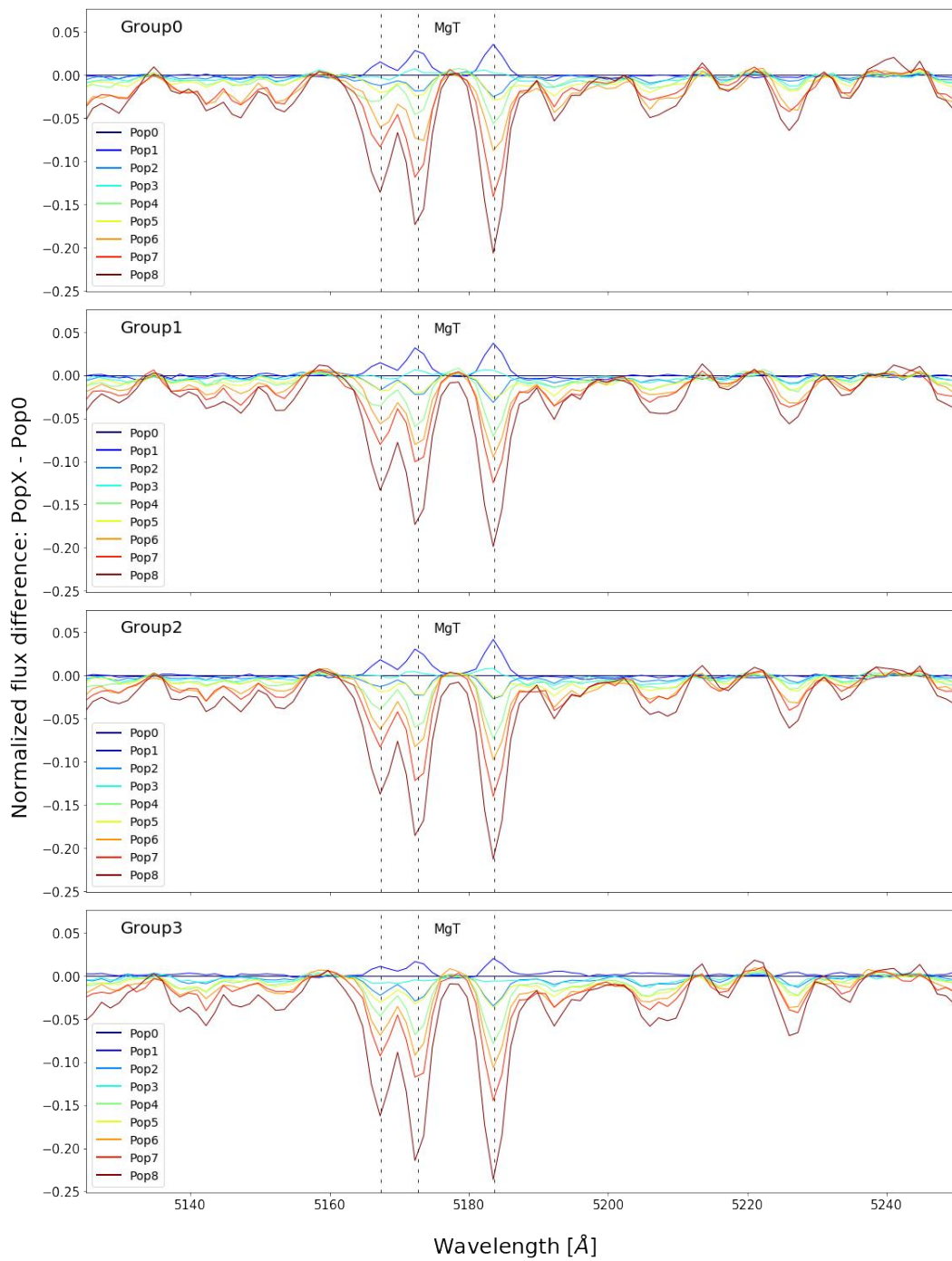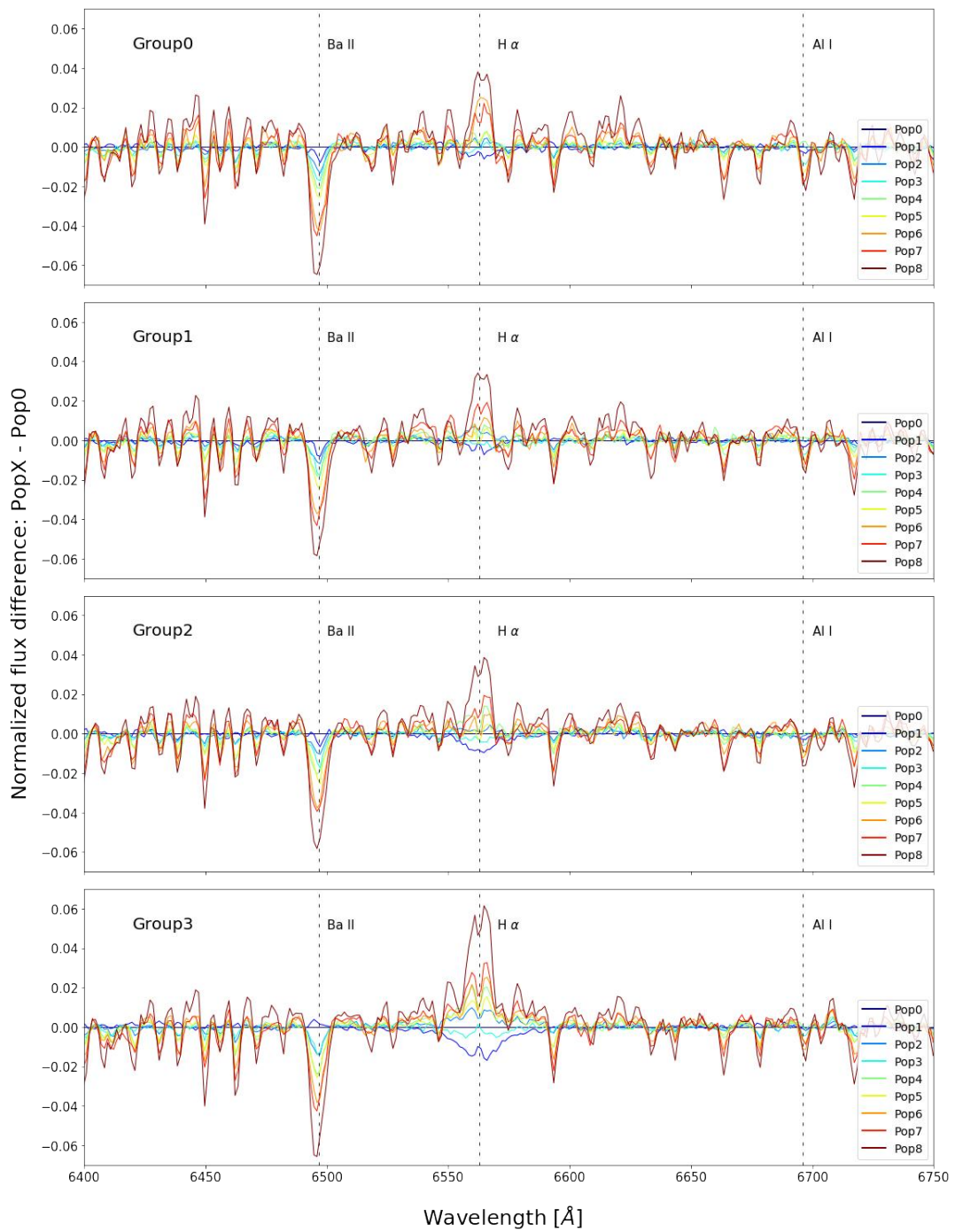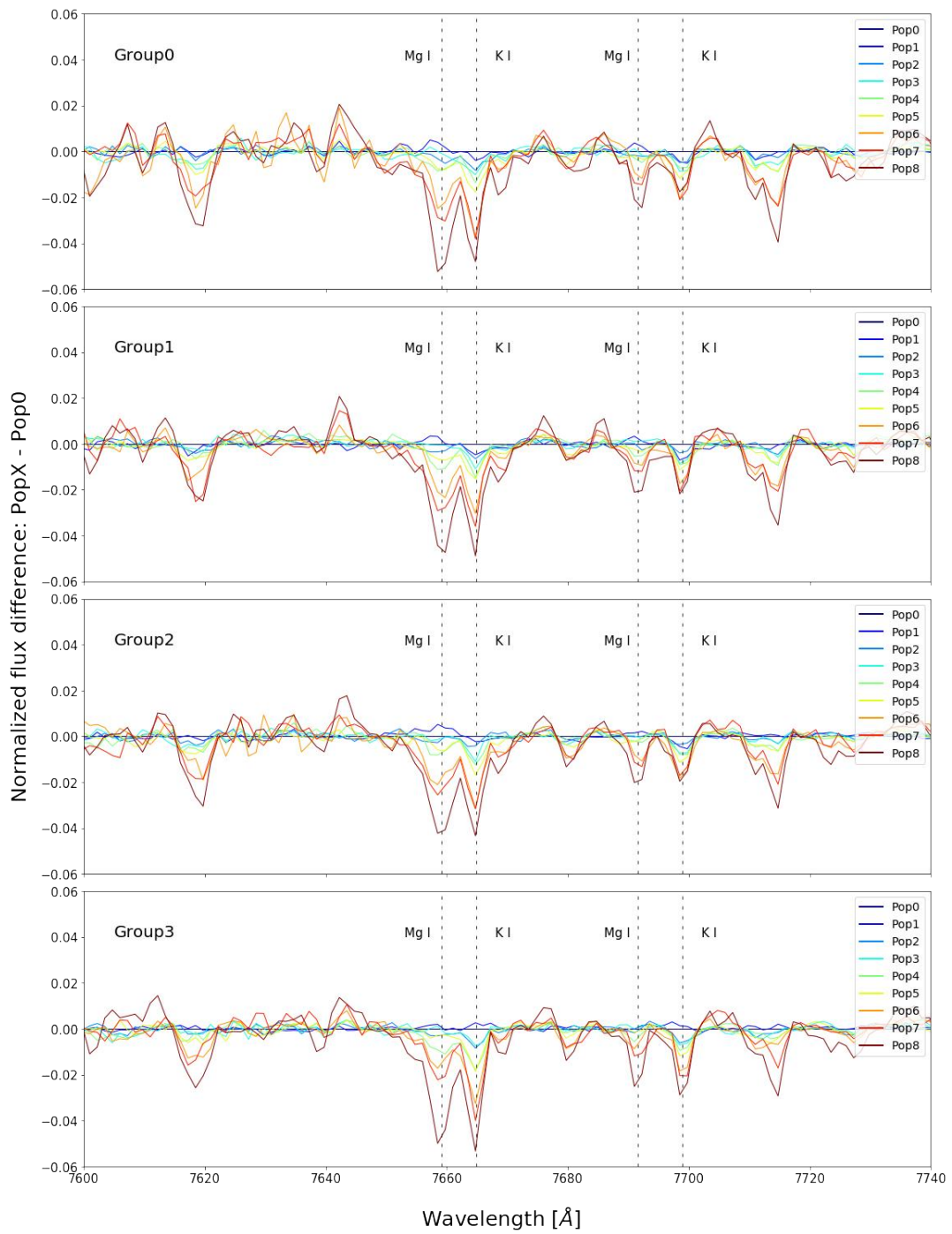
Figure 4.10: Flux difference of each subpopulation with respect to Pop0, in the same wavelength window as Fig. 4.4.
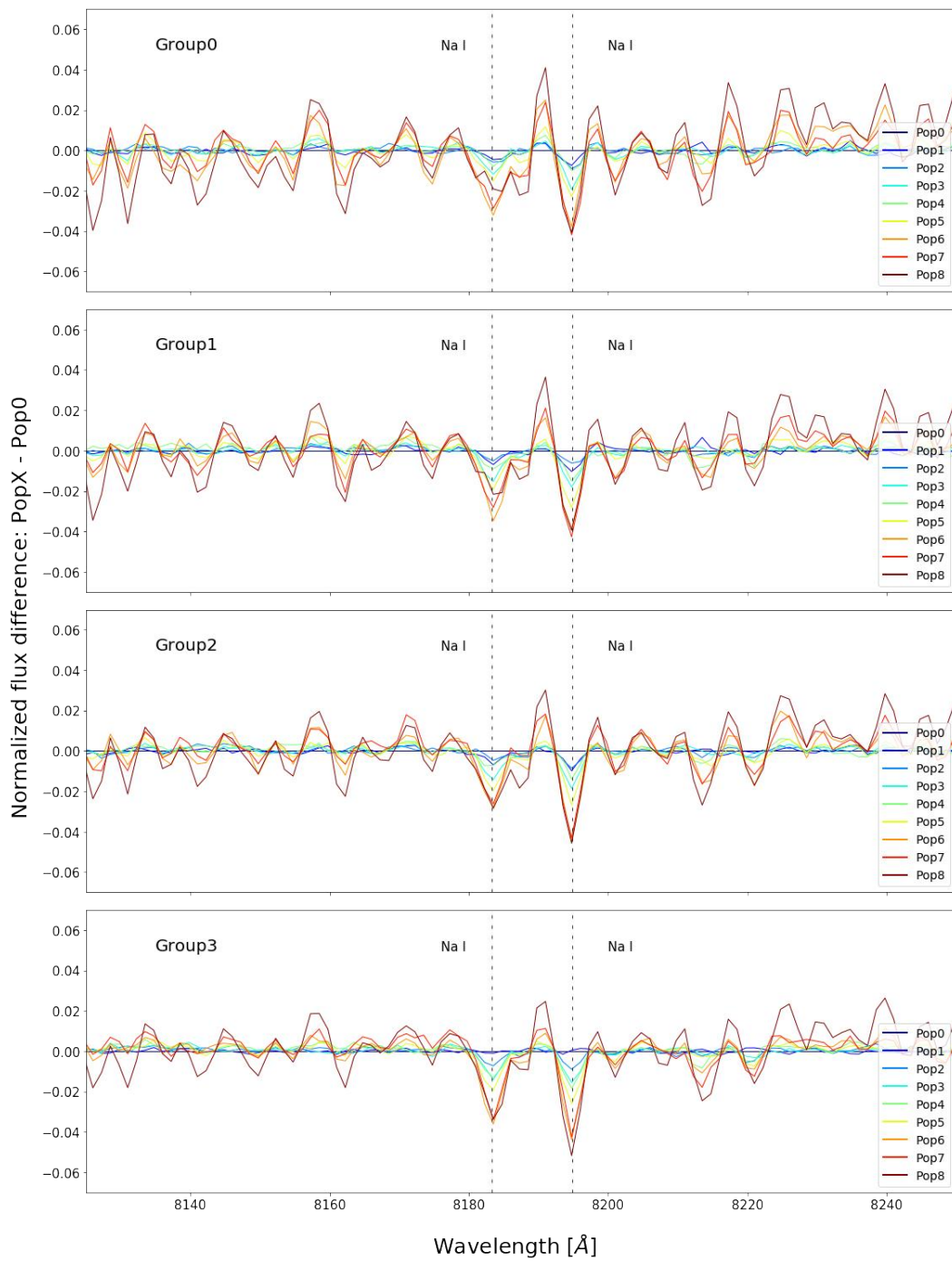
Figure 4.11: Flux difference of each subpopulation with respect to Pop0, in the same wavelength window as Fig. 4.5.
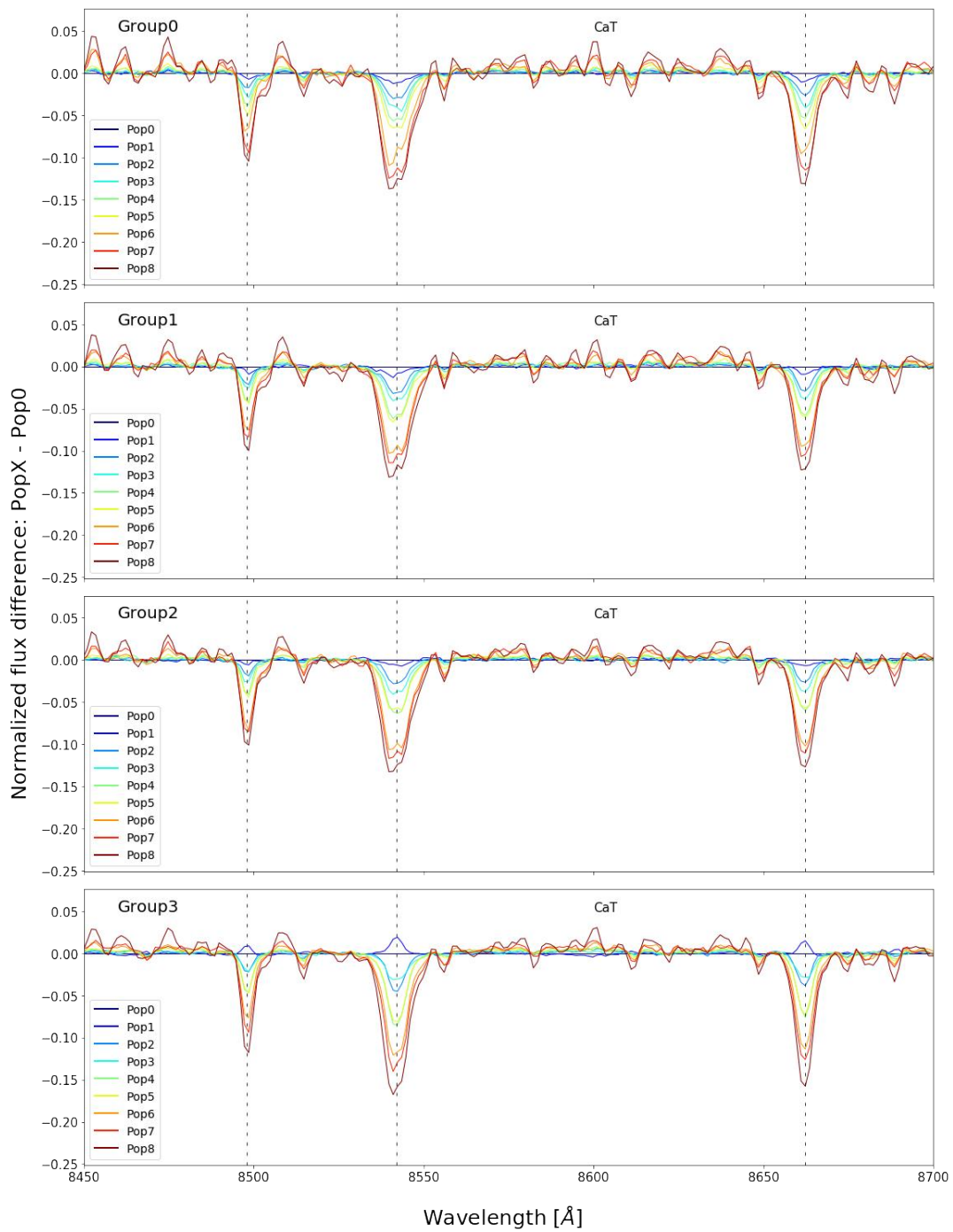
Figure 4.12: Flux difference of each subpopulation with respect to Pop0, in the same wavelength window as Fig. 4.6.

An immediate consideration that follows from the zoomed in spectra (Fig. 4.1, 4.2, 4.3, 4.4, 4.5, 4.6) is that the depth of the absorption lines of metals varies considerably among the populations. The trend of most metal-rich populations having the deepest lines is already appreciable in the Ba lines (Fig. 4.1 and 4.3), but extremely clear in the Mg triplet region (Fig. 4.2), where the spectra split effectively according to their overall metallicity. The same behaviour is confirmed in the other two Mg I lines (Fig. 4.4), where it is also possible to appreciate the split in K I lines, being K an element whose variations have been detected in a few massive GC only: ω Cen, NGC 2419 and NGC 2808 (e.g. Mucciarelli et al. 2012, 2015). The Al I lines (Fig. 4.3) are quite weak; nevertheless, significant differences between the equivalent widths (EWs) of the lines of stellar populations with different metallicities are clearly visible, resulting in a difference between the normalized fluxes of Pop8 with respect to Pop0 of almost 0.02 (Fig. 4.9).

The Ca triplet allows a first sight comparison that is analogous to the case of the Mg triplet. Since the AO gap (see Sect. 2.1.1) prevented the analysis of the Na I doublet, the attention focuses on two other available Na I lines (Fig. 4.5); even though these lines lie in a region where the S/N is not very high even after the stacking, a difference in the line depth is still clear.

These observations are confirmed when plotting the difference in the normalized fluxes with respect to Pop0 (Fig. 4.7, 4.8, 4.9, 4.10, 4.11, 4.12). Intriguingly, these plots reveal that Pop0, the most metal-poor population, is not the one with the shallowest Mg lines: Pop1, that is right after it in order of increasing metallicity, has less deep Mg I lines, a feature that is especially visible in the Mg triplet. Although appropriate comparisons between the observed spectra and grids of synthetic spectra with appropriate chemical composition are needed to derive firm conclusions on the Mg content of the distinct stellar populations, this fact suggests that Pop1 hosts stars that are extremely depleted in Mg. The same happens when comparing other couples of populations: in spite of the increasing metallicity, Pop2 has Mg triplet lines deeper than Pop3, and Pop4 has Mg triplet lines deeper than Pop5. This trend, which is opposite with respect to metallicity, suggests possibly a Mg depletion in Pop3 and Pop5 as well.

Furthermore, a noticeable feature is reported in the Ca triplet window (Fig. 4.12): Pop1 has lines shallower than Pop0, but in Group3 only. This can possibly be explained as a higher He content in Pop1, which exhibits higher temperatures than Pop0 (see Fig. 2.5), even though it has a slightly higher metallicity. As a consequence, when considering fainter stars (Group3), Pop1 approaches a hotter SGB than Pop0, which translates into shallower Ca lines.

As regards the hydrogen lines, the expected behaviour is not to detect a large diversification. Actually, the normalized flux differences reveal a variation in between 0.02

(Group0) and almost 0.06 (Group3) in Hβ of Pop8 (Fig. 4.7), which is probably due to a variation in effective temperature, as it increases in fainter Groups. As a matter of fact, the temperature distribution is wider in populations as Pop0, Pop1 and Pop2 (see Fig. 3.1), which reach higher temperatures in Group3 with respect to the other populations, and hotter stars are likely to exhibit deeper hydrogen absorption lines. This is also confirmed by the wing broadening effect that is visible in Hα and Hβ (Group3) as well as in the Ca triplet.

Most of all, these figures prove that spectral stacking is a promising technique that makes abundance measurements accessible despite the low S/N of the individual MUSE spectra. The resulting stacked spectra are characterized by a S/N that is high enough to detect the weakest lines, as shown by the comparison between Fig. 3.11 and 3.12. After the stacking, Mg I and K I lines, that were not recognizable in the individual spectrum, are deep enough to show an appreciable variation among the different populations. Obviously, the experience proved itself to be more effective with a higher number of stars in the stacked set: as a matter of fact, Pop8 and Pop7, that are the least crowded, consequently have the lowest S/N in their stacked counterparts.

4.2 Further developments

The previous Sect. 4.1 shows that the S/N stacked spectra derived for the distinct stellar populations of ω Cen exhibit high S/N ratio and an unprecedented variety of features. These spectra reveal significant differences between the equivalent widths and the profile of some lines that are crucial to infer the chemical composition of each stellar population. As an example, variations in the spectral lines of Mg, Ba, K, and Ca are clearly detected among the different stellar populations.

A quantitative determination of the elemental abundances of each stellar population would require a large amount of time and a huge effort that is beyond the purposes of this thesis. Nevertheless, the plans for the near future are to use the derived stacked spectra to infer the chemical composition of the stellar populations of ω Cen. To do this, the method developed by Latour et al. (2019) in their study of MPs in the monometallic GC NGC 2808 will be adapted to ω Cen. This method will allow to infer the elemental abundances of various chemical species, including N, O, Na, Mg, Ca and Ba.

In a nutshell, each observed stacked spectrum will be compared with grids of simulated stacked spectra with different chemical composition. Each simulated spectrum will be derived from a collection of synthetic spectra with the same S/N and the same atmospheric parameters and metallicities of the spectra of the individual stars used to derive the observed spectrum. The results will allow to better constrain the chemical enrichment history of ω Cen.

Thanks to the high quality of the available MUSE spectra, the procedure used in this thesis, which consists in combining the spectra of all the stars belonging to a given population obtaining one high S/N ratio spectrum representative of each population, can be extended to SGB and bright MS stars. The synergy of the results obtained from spectroscopy, including the metallicity and the chemical composition, together with the multi-band photometry from HST will allow to identify the distinct stellar populations of ω Cen along different evolutionary stages. Hence, it will be possible to follow each population in the CMD along the bright MS up to the SGB and the RGB.

The comparison between the CMDs of each population and grids of isochrones, which account for the specific chemical composition of each population derived from spectroscopy, will allow to derive accurate and precise age determinations of the multiple stellar populations, thus reconstructing the star formation history of the most massive Galactic GC.

Bibliography

Anderson, A. J. 1997, PhD thesis, University of California, Berkeley

Anderson, J. & van der Marel, R. P. 2010, ApJ, 710, 1032

Arsenault, R., Madec, P. Y., Hubin, N., et al. 2010, in Society of Photo-Optical Instru-
mentation Engineers (SPIE) Conference Series, Vol. 7736, Adaptive Optics Systems II,
ed. B. L. Ellerbroek, M. Hart, N. Hubin, & P. L. Wizinowich, 77360L

Bacon, R., Accardo, M., Adjali, L., et al. 2010, in Society of Photo-Optical Instrumen-
tation Engineers (SPIE) Conference Series, Vol. 7735, Ground-based and Airborne
Instrumentation for Astronomy III, ed. I. S. McLean, S. K. Ramsay, & H. Takami,
773508

Bacon, R., Vernet, J., Borisova, E., et al. 2014, The Messenger, 157, 13

Bastian, N. & Lardo, C. 2018, ARA&A, 56, 83

Baumgardt, H. & Hilker, M. 2018, MNRAS, 478, 1520

Bedin, L. R., Piotto, G., Anderson, J., et al. 2004, Memorie della Societa Astronomica
Italiana Supplementi, 5, 105

Bellini, A., Anderson, J., Bedin, L. R., et al. 2017a, ApJ, 842, 6

Bellini, A., Milone, A. P., Anderson, J., et al. 2017b, ApJ, 844, 164

Bragaglia, A., Carretta, E., Gratton, R. G., et al. 2010, ApJ, 720, L41

Capuzzo-Dolcetta, R. 1993, ApJ, 415, 616

Carnall, A. C. 2017, arXiv e-prints, arXiv:1705.05165

Carretta, E., Bragaglia, A., Gratton, R. G., et al. 2009, A&A, 505, 117

Cottrell, P. L. & Da Costa, G. S. 1981, ApJ, 245, L79

Da Costa, G. S. & Marino, A. F. 2011, PASA, 28, 28

Dantona, F., Gratton, R., & Chieffi, A. 1983, Mem. Soc. Astron. Italiana, 54, 173

Dinescu, D. I., Girard, T. M., & van Altena, W. F. 1999, AJ, 117, 1792

Dotter, A., Chaboyer, B., Jevremović, D., et al. 2008, ApJS, 178, 89

Frebel, A. & Norris, J. E. 2015, ARA&A, 53, 631

Gaia Collaboration, Prusti, T., de Bruijne, J. H. J., et al. 2016, A&A, 595, A1

Gratton, R., Bragaglia, A., Carretta, E., et al. 2019, A&A Rev., 27, 8

Gratton, R. G., Carretta, E., & Bragaglia, A. 2012, A&A Rev., 20, 50

Hilker, M., Kayser, A., Richtler, T., & Willemsen, P. 2004, A&A, 422, L9

Husser, T. O., Wende-von Berg, S., Dreizler, S., et al. 2013, A&A, 553, A6

Ibata, R. A., Bellazzini, M., Malhan, K., Martin, N., & Bianchini, P. 2019, Nature Astronomy, 3, 667

Johnson, C. I. & Pilachowski, C. A. 2010, ApJ, 722, 1373

Joo, S.-J. & Lee, Y.-W. 2013, ApJ, 762, 36

Kamann, S., Husser, T. O., Dreizler, S., et al. 2018, MNRAS, 473, 5591

Kamann, S., Wisotzki, L., & Roth, M. M. 2013, A&A, 549, A71

Latour, M., Calamida, A., Husser, T. O., et al. 2021, A&A, 653, L8

Latour, M., Husser, T. O., Giesers, B., et al. 2019, A&A, 631, A14

Marigo, P., Girardi, L., Bressan, A., et al. 2017, ApJ, 835, 77

Marino, A. F., Milone, A. P., Piotto, G., et al. 2012, ApJ, 746, 14

Marino, A. F., Milone, A. P., Piotto, G., et al. 2009, A&A, 505, 1099

Marino, A. F., Milone, A. P., Renzini, A., et al. 2019, MNRAS, 487, 3815

Massari, D., Koppelman, H. H., & Helmi, A. 2019, A&A, 630, L4

Milone, A. P., Bedin, L. R., Piotto, G., et al. 2008, ApJ, 673, 241

Milone, A. P. & Marino, A. F. 2022, Universe, 8, 359

Milone, A. P., Marino, A. F., Piotto, G., et al. 2015, MNRAS, 447, 927

Milone, A. P., Piotto, G., Renzini, A., et al. 2017, MNRAS, 464, 3636

Mucciarelli, A., Bellazzini, M., Ibata, R., et al. 2012, MNRAS, 426, 2889

Mucciarelli, A., Bellazzini, M., Merle, T., et al. 2015, ApJ, 801, 68

Neumayer, N., Seth, A., & Böker, T. 2020, A&A Rev., 28, 4

Nitschai, M., Neumayer, N., Clontz, C., et al. 2023, submitted to ApJ

Norris, J. E. & Da Costa, G. S. 1995, ApJ, 447, 680

Norris, J. E., Freeman, K. C., & Mighell, K. J. 1996, ApJ, 462, 241

Pechetti, R., Kammann, S., Krajnovic, D., et al. 2023, submitted to MNRAS

Pfeffer, J., Lardo, C., Bastian, N., Saracino, S., & Kamann, S. 2021, MNRAS, 500, 2514

Piotto, G., Villanova, S., Bedin, L. R., et al. 2005, ApJ, 621, 777

Renzini, A. & Buzzoni, A. 1986, in Astrophysics and Space Science Library, Vol. 122,
    Spectral Evolution of Galaxies, ed. C. Chiosi & A. Renzini, 195–231

Seth, A. C., Dalcanton, J. J., Hodge, P. W., & Debattista, V. P. 2006, arXiv e-prints,
    astro

Ströbele, S., La Penna, P., Arsenault, R., et al. 2012, in Society of Photo-Optical Instru-
    mentation Engineers (SPIE) Conference Series, Vol. 8447, Adaptive Optics Systems III,
    ed. B. L. Ellerbroek, E. Marchetti, & J.-P. Véran, 844737

Tailo, M., D'Antona, F., Vesperini, E., et al. 2015, Nature, 523, 318

VandenBerg, D. A., Richard, O., Michaud, G., & Richer, J. 2002, ApJ, 571, 487

Villanova, S., Geisler, D., Gratton, R. G., & Cassisi, S. 2014, ApJ, 791, 107

Weilbacher, P. M., Palsa, R., Streicher, O., et al. 2020, A&A, 641, A28

Weilbacher, P. M., Streicher, O., & Palsa, R. 2016, MUSE-DRP: MUSE Data Reduction
    Pipeline, Astrophysics Source Code Library, record ascl:1610.004